Unit cell simulations and porous plasticity modelling for strongly anisotropic FCC metals

Lars Edvard Bryhni Dæhli[a,b,*], Jonas Faleskog[c], Tore Børvik[a,b], Odd Sture Hopperstad[a,b]

[a]*Structural Impact Laboratory (SIMLab), Department of Structural Engineering, Norwegian University of Science and Technology (NTNU), NO-7491 Trondheim, Norway*
[b]*Centre for Advanced Structural Analysis (CASA), NTNU, NO-7491 Trondheim, Norway*
[c]*Department of Solid Mechanics, Royal Institute of Technology (KTH), SE-100 44 Stockholm, Sweden*

Abstract

The macroscopic behaviour of anisotropic porous solids made from an aggregate of spherical voids embedded in a plastically anisotropic matrix material is investigated by means of unit cell simulations. Plastic yielding of the polycrystalline matrix is governed by the anisotropic yield criterion Yld2004-18p. Generic texture components for face-centred cubic crystals resembling those that typically emerge during rolling and annealing processes are applied in the study. A numerical method for systematic prescription of external stress states is presented and employed in the unit cell calculations. To preclude shear effects in the unit cell model, the material symmetry axes are restricted to coincide with the principal stress directions. This excludes the possibility to properly study the ductile failure mechanism and the current work is thus mainly concerned with the void growth phase. Various stress states ranging from biaxial tension to highly constrained regions in the vicinity of crack tips are employed in the study. The numerical results demonstrate that the matrix anisotropy has a marked effect on the unit cell response, both in terms of void growth and stress-strain curves. Furthermore, the void shape evolves quite differently depending upon the direction of the major principal stress relative to the material axes. A heuristic extension of the Gurson model that incorporates matrix plastic anisotropy is presented and subsequently used to describe the constitutive behaviour of the porous ductile solid. Numerical data from the unit cell analyses are used as target curves in the calibration process of the porous plasticity model. A sequential least-square optimization procedure is invoked to minimize the overall discrepancy between the unit cell calculations and the homogenized response of the plastically anisotropic porous solid for all the imposed stress states. The anisotropic porous plasticity model demonstrates predictive capabilities for the range of stress states covered in this study.

Keywords: Unit cell modelling; Porous plasticity; Plastic anisotropy

1. Introduction

Most structural metals exhibit some degree of anisotropy and initially isotropic wrought alloys will develop texture during deformation leading to plastically anisotropic behaviour. For instance, forming operations that are typically applied in the production of materials for structural applications impose directional dependencies in the material. One such forming process is the rolling of sheet metals which results in deformation texture for which orthotropic plastic anisotropy may be assumed. In the case of face-centred cubic (FCC) metals, such as aluminium-based alloys, the deformation texture is usually composed of the generic textures brass, copper and S. If the metal sheet is further exposed to an annealing process, the textures that remain may be taken as a combination of the cube texture, and to a lesser extent, the Goss texture (Barlat and Richmond, 1987). Because sheet metal alloys are often used in structural applications, for instance in the aerospace (plane skins), military (protective structures), automotive (car body parts) and construction industries (building facades), predictive modelling of these materials is of great concern in terms of cost reduction and integrity assessment.

Structures are often designed for situations in which ductile failure should be circumvented. Under such circumstances, material softening and damage progression may be disregarded and one can use the constitutive models derived

---

*Corresponding author
Email address:* `lars.e.dahli@ntnu.no` (Lars Edvard Bryhni Dæhli)

for polycrystalline solids without the consideration of particles and voids, although the latter two are inherent to the material microstructure. Many anisotropic yield criteria suited for polycrystalline metal alloys have been proposed throughout the literature. Perhaps one of the most fundamental and well-known anisotropic descriptions was proposed by Hill (1948). Being based on a quadratic yield surface, however, it is known to provide somewhat inaccurate estimates for the plastic yielding of aluminium alloys, as have been demonstrated by experiments (Woodthorpe and Pearce, 1970; Stout et al., 1983; Iadicola et al., 2008) and by polycrystal simulations (Bishop and Hill, 1951; Hutchinson, 1964). A yield criterion for orthotropic anisotropy was proposed by Barlat et al. (1991) based on an extension of the non-quadratic yield surface by Hershey (1954) and Hosford (1972). To accommodate the most general form of anisotropy, a highly flexible model that was founded on the use of linear transformations of the stress tensor was initially proposed by Karafillis and Boyce (1993). In the spirit of their work, other models were later proposed by for example Bron and Besson (2004), Barlat et al. (2005), and Plunkett et al. (2008). The latter is also able to account for tension-compression asymmetry, which is important for materials that display strength-differential effects caused by for instance twinning or non-Schmid effects. The above non-quadratic anisotropic yield criteria have demonstrated predictive capabilities in a vast number of studies throughout the literature, and they constitute a broad and general framework for phenomenological modelling of plastically anisotropic solids.

The ductile failure process of metal alloys is in many situations governed by the nucleation, growth and coalescence of microsized voids within the material leading to local material degradation and final fracture. Modelling of this type of materials is often attempted using homogenized material models that are micromechanically motivated and based on the Hill-Mandel homogenization theory (Mandel, 1966; Hill, 1967). These models are referred to as porous plasticity models in the following. At the homogenized material level, porous plasticity models are able to capture material softening through an appropriate evolution of some microstructural variables included in the model. These variables must account for typical phenomena that occur at a lower scale during ductile fracture. Perhaps the best known model that is founded on a micromechanical basis was proposed in the seminal work of Gurson (1977). The attractiveness of this model resides in its rather simple formulation and implementation, only incorporating a single microstructural parameter through the volume fraction of microscopic voids, and its closed-form formulation. The Gurson model was later suitably modified by Tvergaard (1981) to enhance the predictions as compared to unit cell calculations, and this is today the extension of the model which has received most attention in the literature. Over the past three decades, a great number of porous plasticity models have spawned from Gurson's original development, especially in the case of isotropic matrix materials. A review of these models is outside the scope of this paper, and the reader is advised to consult recent review papers by Benzerga and Leblond (2010), Besson (2010), or Benzerga et al. (2016) for detailed expositions of the advances within the context of porous plasticity modelling.

Previous studies have shown that ductile failure is influenced by the directional dependency of anisotropic solids (see for example Jordon et al. (2009), Luo et al. (2012) and Fourmeau et al. (2013)). Several studies have made advances towards including plastic anisotropy in damage models of ductile failure (see for instance Chow and Wang (1987); Brünig et al. (2008); Luo et al. (2012)). Also within the context of porous plasticity modelling there have been made quite a few efforts over the past two decades. However, the number of porous plasticity models for anisotropic materials is still more sparse than for isotropic materials. To the best knowledge of the authors, the first upper-bound analysis was undertaken by Liao et al. (1997) who extended the cylindrical Gurson model (Gurson, 1977) for an anisotropic porous sheet under plane stress conditions and in-plane isotropy based on Hill's anisotropic yield criterion (Hill, 1948). Liao et al. (1997) also proposed a potential modification of their cylindrical model to account for a spherical representative volume element (RVE) by considering the similarities between the cylindrical and the spherical isotropic yield functions proposed by Gurson (1977). Chien et al. (2001) later modified this model by introducing the q_i parameters along the same lines as Tvergaard (1981). Wang et al. (2004) employed the same porous plasticity model but included an average anisotropy coefficient in the yield function to accommodate planar anisotropy. Benzerga and Besson (2001) derived macroscopic yield functions using upper-bound limit analyses for a Hill (1948) matrix description under more general situations, meaning without restriction to in-plane isotropy, for both cylindrical and spherical RVEs. Benzerga et al. (2002, 2004) extended the resulting porous plasticity model in a heuristic manner to simultaneously account for void shape effects and plastic anisotropy. This was enabled by a suitable combination with some salient features of the GLD model (Gologanu et al., 1993) to account for the initial void shape. Monchiet et al. (2008) derived closed-form expressions for the macroscopic yielding of a representative volume element (RVE) comprising spheroidal voids embedded in a Hill matrix. Later, Keralavarma and Benzerga (2010) provided an analytical criterion for a porous ductile solid in the case of Hill's anisotropic yield criterion and spheroidal voids, however applicable to non-axisymmetric

loadings and in situations where the void axes may differ from the material axes of orthotropy. Stewart and Cazacu (2011) considered an orthotropic yield criterion exhibiting tension-compression asymmetry (Cazacu et al., 2006) in the homogenization procedure. Although this matrix description generally accounts for non-quadratic yield surfaces, the derivation in Stewart and Cazacu (2011) was restricted to situations where the yield surface was indeed of a quadratic character, however accounting for plastic anisotropy. Recently, Morin et al. (2015) presented a yield criterion based on a Gurson-type approach, but suitably modified to account for both plastic anisotropy and ellipsoidal voids. A similar criterion for an isotropic matrix description was successfully employed to predict the ductile failure under predominantly shear stress states (Morin et al., 2016) as compared to unit cell simulations.

Although the development of the above-mentioned models is more involved and physically founded than the model proposed in the present study, they are somewhat restrained by the use of Hill's anisotropy criterion which does not provide reliable descriptions of plastic flow for anisotropic polycrystalline solids in general (Woodthorpe and Pearce, 1970; Stout et al., 1983; Iadicola et al., 2008). However, to derive yield functions for voided materials based on the upper-bound analysis undertaken by Gurson (1977) is in general a difficult task. By adding complexities in the matrix formulation, such as more advanced anisotropic yield criteria, the task may become unmanageable except for some very limited loading configurations. Moreover, even though the ability to properly describe the evolution of the approximated microstructure through rigorous development of porous plasticity models from upper-bound limit analysis is of great importance, it seems that from an engineering perspective the ability to for instance correctly predict the thickness reduction of a sheet overshadows the ability to quantify the porosity within the material.

A more pragmatic way of including anisotropy into the porous plasticity framework was seemingly first proposed by Doege and Seibert (1995) to predict necking and wrinkling in sheet-metal forming. The same model was later used by Prat et al. (1998) and Grange et al. (2000) to model the mechanical behaviour of a zirconium alloy used in the nuclear industry. More recently, Chen and Dong (2009) conducted a number of single element and benchmark tests on this porous plasticity model using explicit finite element simulations. In addition, Brunet et al. (1998) adopted a similar porous plasticity model to study necking in sheet metal forming processes. They also extended the formulation to account for non-quadratic anisotropic yield surfaces. Later, Steglich et al. (2010) used the same heuristic extension of the Gurson model, albeit accommodating more general forms of anisotropy by substituting the von Mises equivalent stress with the anisotropic equivalent stress measure proposed by Bron and Besson (2004). This type of model has also recently been successfully applied in a study by Shinohara et al. (2016). Similar ways of incorporating various effects into the Gurson model have been presented by Gao et al. (2011). They considered effects of both the third deviatoric stress invariant and a non-associated flow rule by heuristic modification of the Gurson model.

Studies dealing with unit cell simulations involving plastically anisotropic matrix descriptions have been reported in the literature, however less frequently than for isotropic materials. Benzerga and Besson (2001) conducted axisymmetric unit cell simulations under proportional loading paths to assess the performance of their proposed model. Three-dimensional unit cell simulations with an anisotropic Hill (1948) matrix formulation were undertaken by Chien et al. (2001) and Wang et al. (2004) for a cubic material block with a triply periodic array of spherical voids to validate the porous plasticity model by Liao et al. (1997). In their assessment of ductile failure for an aluminium alloy sheet metal, Steglich et al. (2010) carried out three-dimensional unit cell simulations under a rather wide range of proportional stress states where the anisotropic yield criterion by Bron and Besson (2004) was used for the matrix. Contributions have also been made by Keralavarma and Benzerga (2010) and Keralavarma et al. (2011) using axisymmetric unit cell calculations for various anisotropic matrix materials. Recently, Shinohara et al. (2016) published a paper in which three-dimensional unit cell simulations were conducted for a high-strength steel, however restricted to states of generalized tension. These studies report on significant dependencies of the unit cell response upon the matrix anisotropy. In a very similar manner, three-dimensional unit cell analyses have been performed for single crystals (Yerra et al., 2010; Han et al., 2013; Srivastava and Needleman, 2013, 2015), which are inherently anisotropic due the discrete nature of the plastic slip.

The aim of this paper is to first present a numerical framework for conducting unit cell simulations in the case of plastically anisotropic solids where the imposed stress state can be controlled by the user. This requires consideration of the entire deviatoric stress space, since anisotropic yield surfaces are in general not required to possess any symmetries. Further, this numerical framework will be used to investigate the macroscopic response of a porous solid represented by a spherical void embedded in a cube made up of a plastically anisotropic matrix. Plastic yielding of the matrix is governed by a phenomenological anisotropic yield criterion (Barlat et al., 2005) for which the predictive capabilities have been proven for different aluminium alloys (Achani et al., 2009, 2011). Both the exponent of the yield criterion

and the directional dependency induced by plastic anisotropy have noticeable impact on the mechanical response of the unit cell models. Furthermore, building upon the work by Doege and Seibert (1995) and Steglich et al. (2010), we propose a porous plasticity model accounting for the plastic anisotropy of the matrix material in a heuristic manner. The anisotropic porous yield criterion reduces to the Yld2004-18p yield criterion in the limit of zero porosity. The last part of the paper deals with calibration of the porous plasticity model. In this work, the unit cell simulations will be used as reference curves for the optimization procedure. The optimization results show that the porous plasticity model employed in the current investigation is able to account for the macroscopic response of the assumed microstructure, and as such is regarded amenable for practical usage. However, a validation against data from physical experiments is not carried out herein but is considered to be an important part for further studies.

2. Matrix material description

2.1. Constitutive model

The matrix material is governed by a hypoelastic-plastic formulation, in which the rate-of-deformation tensor is additively split into elastic and plastic parts, namely

$$\hat{\mathbf{d}} = \hat{\mathbf{d}}^{\text{e}} + \hat{\mathbf{d}}^{\text{p}} \tag{1}$$

A corotated formulation is used to account for arbitrarily large deformations and rotations, and the notation $(\hat{\circ})$ is used to denote corotated tensors. The corotated frame is defined such that it corresponds to the basis spanned by the axes of anisotropy, referred to as material axes in the following, and the Cartesian base vectors used to express the tensor components are thus understood to rotate with the material axes during deformation. Due to the hypoelastic formulation and under the assumption of isotropic elasticity, the generalized Hooke's law is utilized to relate the corotated stress rate and the elastic rate-of-deformation, such that

$$\dot{\hat{\boldsymbol{\sigma}}} = \frac{E}{1 + \nu} \hat{\mathbf{d}}'^{\text{e}} + \frac{E}{3 \, (1 - 2\nu)} \text{tr}(\hat{\mathbf{d}}^{\text{e}}) \mathbf{1} \tag{2}$$

Here, the deviatoric and volumetric parts of the elastic rate-of-deformation tensor are denoted $\hat{\mathbf{d}}'^{\text{e}}$ and $\text{tr}(\hat{\mathbf{d}}^{\text{e}})$, respectively, while $\mathbf{1}$ is the identity tensor. Values of the elastic modulus E and the Poisson ratio ν are provided in Table 1 for the generic matrix descriptions adopted throughout this study.

The plastic response of the matrix is governed by the Yld2004-18p anisotropic yield criterion Barlat et al. (2005). This is a phenomenological anisotropic yield criterion that is appropriate to describe the quite pronounced textures applied in this study. The Yld2004-18p yield criterion is based on two linear transformations of the corotated deviatoric stress tensor $\hat{\boldsymbol{\sigma}}'$ given by

$$\hat{\mathbf{s}}^{(1)} = \hat{\mathbf{A}}^{(1)} : \hat{\boldsymbol{\sigma}}' \quad \wedge \quad \hat{\mathbf{s}}^{(2)} = \hat{\mathbf{A}}^{(2)} : \hat{\boldsymbol{\sigma}}' \tag{3}$$

where $\hat{\mathbf{s}}^{(1)}$ and $\hat{\mathbf{s}}^{(2)}$ are the transformed deviatoric stress tensors, and $\hat{\mathbf{A}}^{(1)}$ and $\hat{\mathbf{A}}^{(2)}$ are the fourth order transformation tensors that account for plastic anisotropy. An equivalent stress measure is further defined on the form

$$\sigma_{\text{eq}} = \left(\frac{1}{4} \sum_{i=1}^{3} \sum_{j=1}^{3} |\hat{s}_i^{(1)} - \hat{s}_j^{(2)}|^m \right)^{\frac{1}{m}} \tag{4}$$

with $\hat{s}_i^{(1)}$ and $\hat{s}_j^{(2)}$ denoting the principal values of the transformed corotated stress deviator, and m being an exponent that governs the curvature of the yield surface. The reader is referred to Barlat et al. (2005) for a more comprehensive description of the anisotropic yield function.

Plastic yielding of the matrix material is governed by the yield criterion

$$\phi \, (\hat{\boldsymbol{\sigma}}, \sigma_{\text{M}}) = \sigma_{\text{eq}} - \sigma_{\text{M}} = 0 \tag{5}$$

4

Table 1: Generic material parameters used for the matrix.

E [GPa]	ν	σ_0 [MPa]	Q [MPa]	C
70	0.3	100	100	10

We employ an associated flow rule in this study, and the plastic rate-of-deformation tensor reads

$$\hat{\mathbf{d}}^{\mathrm{P}} = \dot{\lambda}\frac{\partial \phi}{\partial \hat{\sigma}} \tag{6}$$

where $\dot{\lambda}$ is the plastic parameter. The flow stress of the matrix material is described by a one-term Voce rule on the form

$$\sigma_{\mathrm{M}} = \sigma_0 + Q\left(1 - \exp\left(-Cp\right)\right) \tag{7}$$

with the material parameters listed in Table 1. These matrix material parameters are arbitrarily chosen for the purpose of keeping the study generic, but they are representative of strain hardening parameters for typical low-hardening commercial aluminium alloys. The accumulated plastic strain is calculated from the plastic work rate, such that

$$p = \int_0^t \dot{p}\,\mathrm{d}t, \quad \dot{p} \equiv \frac{\hat{\sigma} : \hat{\mathbf{d}}^{\mathrm{P}}}{\sigma_{\mathrm{eq}}} = \dot{\lambda} \tag{8}$$

The latter equality follows from the associated flow rule and the fact that σ_{eq} is a first-order homogeneous function with respect to the stress.

We used a material user subroutine (UMAT) in Abaqus/Standard for temporal integration of the matrix rate constitutive equations. In the case of plastic loading steps, a semi-implicit backward-Euler integration scheme (Belytschko et al., 2000) was used to update the stress state. We employed substepping of the strain increments to ensure sufficient accuracy of the integration point values by enforcing a threshold value for the increment in equivalent deviatoric strain. If the norm of deviatoric strain increment was larger than a given threshold value

$$\Delta\bar{\varepsilon} = \Delta t \sqrt{\hat{\mathbf{d}}' : \hat{\mathbf{d}}'} > 0.05\sigma_0/E \tag{9}$$

the strain increment being fed to the subroutine from the FE solver was split into N_s number of substeps such that $\Delta\bar{\varepsilon}^* = \Delta\bar{\varepsilon}/N_s$. The number of substeps was then determined as the least integer that gives $\Delta\bar{\varepsilon}^* \leq 0.05\sigma_0/E$. Note that this only subdivides the strain increments inside the material subroutine into smaller steps, while the global increments are not affected.

2.2. Calibration of the anisotropy parameters

Six generic crystallographic textures are employed in this study to enforce different types of matrix anisotropy. These are the so-called brass, copper, S, cube, Goss, and random textures. The first five are representative of the typical texture components found in FCC polycrystals. More specifically, the brass, copper, and S textures are usual components for deformation textures, while the cube and Goss are texture components that typically remain after annealing (Barlat and Richmond, 1987). The random texture is representative for an isotropic material with a high-exponent yield surface, and is included such that pure anisotropy effects may be discerned from the influence of a non-quadratic yield surface associated with the plasticity model described in Section 2.1. However, due to geometrical effects imposed by the void, even in the case of an isotropic matrix, large deformations will lead to morphological anisotropy due to void shape changes. For details regarding the various textures the reader is encouraged to consult Engler and Randle (2010).

Each generic texture, except the random texture, comprised 50% pure component with a scatter width of 5° around its ideal component, and the remaining 50% randomly distributed. The random texture was made up from an entirely random distribution of grain orientations. Numerical simulations based on the full-constraint (FC) Taylor method were

used to calculate yielding points in stress space. The yielding points were defined by pre-chosen values of specific plastic work, in this particular case set to $W^p = 0.35$ MPa, which corresponds to a proof strain of about 0.2%. A total of 1600 grains were used in the homogenization procedure. The reader is referred to Saai et al. (2013, 2014) for further details on the computational homogenization procedure.

Plane stress states were considered in the FC Taylor calculations by imposing in-plane velocities. We note that this somewhat reduces the generality of the matrix anisotropy since the material parameters governing out-of-plane shear stresses cannot be determined and are consequently set to unity. However, the intent of the current work is to compare numerical results obtained with a discretized microstructure represented by a unit cell and a homogenized porous plasticity model, and the anisotropy parameters determined from these plane stress data points suffice to convey the main observations and make a quantitative comparison. As such, we emphasize that the numerical results from the FC Taylor simulations are not important for the present investigation, and they should be merely considered to constitute a data set which was used to describe different anisotropy parameters for the phenomenological yield criterion. Consequently, results from these calculations are not presented herein.
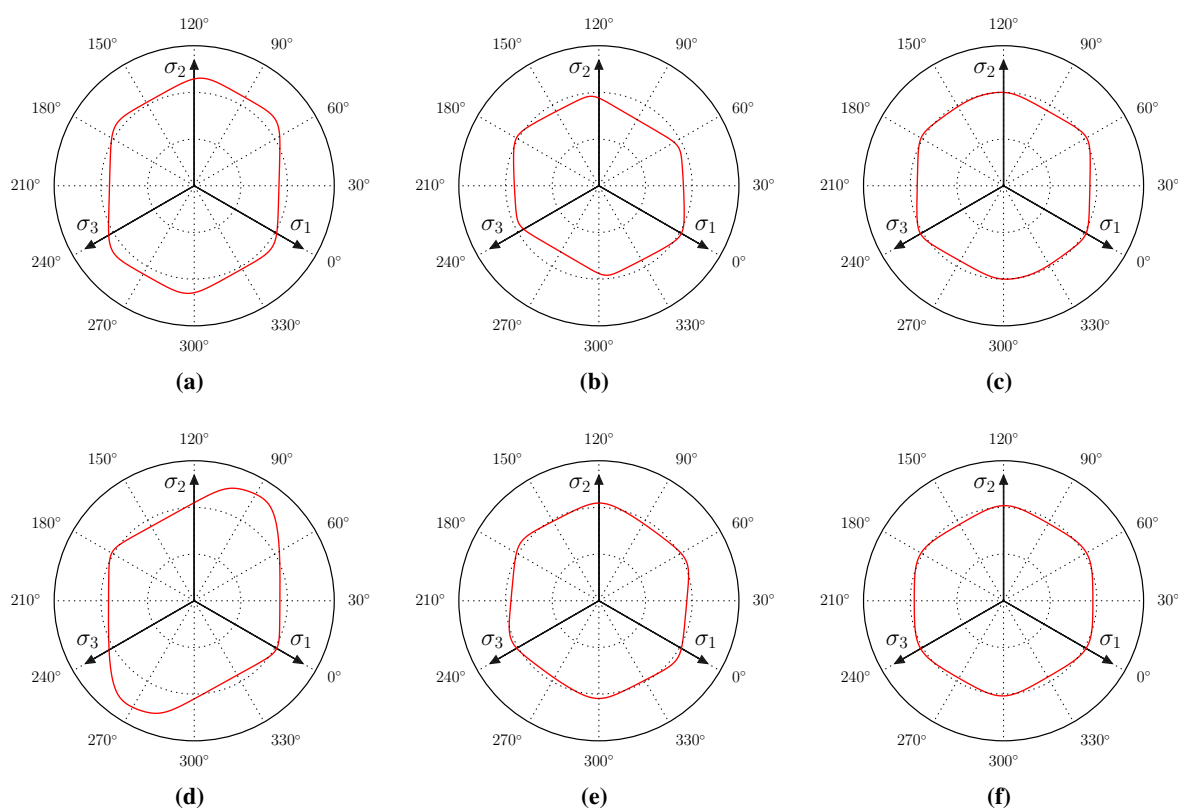

Figure 1: Yld2004-18p yield surfaces for the generic textures plotted in the deviatoric stress plane when the material axes $\mathbf{m}_i$ are aligned with the principal stress directions. The subfigures pertain to the (a) brass, (b) copper, (c) cube, (d) Goss, (e) S, and (f) random textures, respectively. Deviatoric angles $\theta = 0°$, $120°$, and $240°$ correspond to the σ_1-axis, σ_2-axis, and σ_3-axis, as indicated in the figures.

To describe the plastic anisotropy analytically, a total number of 500 distinct yielding points determined from the FC Taylor calculations were used to calibrate the Yld2004-18p constitutive model. The quantitative correspondence between the FC Taylor simulations and the calibrated Yld2004-18p criterion was reasonably good for all textures. The reader is referred to Saai et al. (2014) for a more elaborate discussion of this matter. The anisotropy coefficients entering the transformation tensors $\hat{\mathbf{A}}^{(1)}$ and $\hat{\mathbf{A}}^{(2)}$ in Equation (3) are given in Appendix A. Figure 1 shows plots of the resulting yield surfaces for all the investigated textures in the deviatoric plane. In these illustrations, the axes of material symmetry $\mathbf{m}_i$ are collinear to the principal stress directions. Specifically, the rolling direction (RD) $\mathbf{m}_1$ is aligned with

the σ_1-axis, the transverse direction (TD) $\mathbf{m}_2$ with the σ_2-axis, and the normal direction (ND) $\mathbf{m}_3$ with the σ_3-axis.

We note that the evolution of the texture with plastic deformation is not accounted for in the present work, and the initial anisotropy is assumed throughout the numerical simulations. Effects of anisotropy evolution might be important, at least in the context of ductile failure and localization of plastic deformation (Yoshida and Kuroda, 2012), and efforts towards including such effects could be attempted in future work.

3. Unit cell modelling

Unit cell simulations are conducted to investigate the mechanical response of an initially voided material with a plastically anisotropic matrix representing the material at the microstructural level. The matrix material is modelled by the Yld2004-18p yield criterion presented in Section 2.1 which is taken to represent the generic textures from Section 2.2.

3.1. Representative volume element and finite element model

The representative volume element used in the unit cell study is a cube with an initially spherical void located at its centre. This corresponds to a uniform distribution of equally spaced spherical voids. It is then realized that effects of the initial spatial distribution and void shape are neglected, which may have pronounced effects on the ductile failure process (Pardoen and Hutchinson, 2000). However, the emphasis of this study is restricted to effects of matrix anisotropy and yield surface curvature.

To preclude shear effects in the numerical simulations, the material axes $\mathbf{m}_i$ are chosen to globally coincide with the principal directions of both stress and strain. Consequently, the unit cell is loaded only by normal stress components. Symmetry conditions are then exploited in order to model only 1/8 of the entire RVE, which greatly reduces the computational cost of the simulations. The chosen RVE and the corresponding discretized unit cell model are shown in Figure 2a and Figure 2b, respectively. In all simulations, the unit cell geometry is defined by $L_1 = L_2 = L_3 = 2\bar{L}$, where $\bar{L}$ is the edge length employed in the 1/8 model. Initially, the void radii are equal along all three coordinate axes, such that $R_1 = R_2 = R_3 = \bar{R}$. Hence, the initial void volume fraction is defined by

$$f_0 = \frac{V_{\mathrm{v}}}{V_{\mathrm{RVE}}} = \frac{\pi \bar{R}^3}{6\bar{L}^3} \tag{10}$$

where V_{v} and V_{RVE} denote the volume of the void and the RVE, respectively. An initial void content of $f_0 = 0.005$ was used in all simulations, thus excluding the possibility to investigate effects of the initial porosity on the mechanical behaviour. The chosen void volume fraction, however, is deemed representative for the combined content of initial voids and primary void-nucleating particles in typical aluminium alloys (see for example Westermann et al. (2014)).

Periodic boundary conditions are assigned to the unit cell by restricting the external boundaries to remain straight throughout the analyses. Nonlinear kinematical constraints were utilized to accommodate full control of the imposed stress state, and are specifically intended to ensure that the global loading state of the unit cell remains proportional throughout the analysis. This is treated in detail in Appendix B.1. Implicit finite element (FE) simulations were carried out using ABAQUS/Standard 6.13 (Abaqus, 2013). A mesh convergence study was carried out on beforehand to ensure that the unit cell response was adequately described by the FE model. The details of that study, however, will be omitted here. We found that a unit cell configuration consisting of 1282 second-order hexagonal elements with reduced integration (C3D20R) gave an adequate representation of the mechanical response. This spatial discretization was used for all unit cell simulations presented in the following.

3.2. Macroscopic stress state

A systematic prescription of the macroscopic loading is crucial to elucidate and interpret effects of the imposed stress state on the overall unit cell response. To describe the stress state concisely, let us begin by considering an arbitrary point in the principal stress space. This stress point is denoted P in Figure 3a. The normal vector $\mathbf{n}$ denotes the hydrostatic axis, and the radius r in the deviatoric plane is related to the stress deviator and the von Mises equivalent stress through

$$r = \sqrt{\boldsymbol{\Sigma}' : \boldsymbol{\Sigma}'} = \sqrt{2J_2} = \sqrt{\frac{2}{3}} \Sigma_{\mathrm{eq}}^{\mathrm{vm}} \tag{11}$$
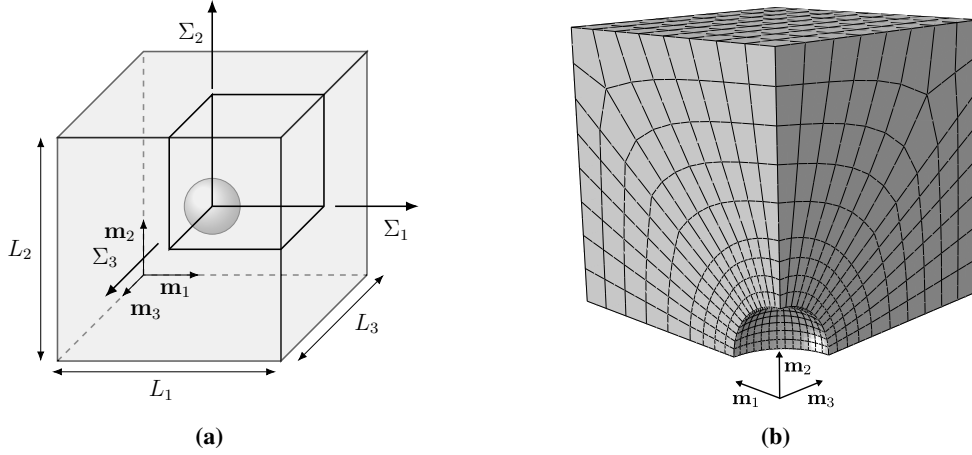
7

Figure 2: Illustration of (a) the representative volume element, and (b) the corresponding FE model of the discretized 1/8 unit cell. The material axes $\mathbf{m}_i$ are collinear to the macroscopic principal stress directions.

Here, $\boldsymbol{\Sigma}'$ is the macroscopic stress deviator, J_2 denotes the second principal invariant of the stress deviator, and $\Sigma_{\mathrm{eq}}^{\mathrm{vm}}$ refers to the equivalent von Mises stress. Note that we now use capital letters to indicate that these are macroscopic quantities applied to the unit cell model. Figure 3b illustrates the same stress state projected into the deviatoric plane, where the deviatoric angle θ is defined as the angle between the Σ_1-direction and the stress point P in the projected plane.

Decomposing the stress tensor into deviatoric and hydrostatic parts, we may now make use of Equation (11) and the deviatoric angle to write the principal stress components on vector form as

$$
\begin{aligned}
\begin{Bmatrix} \Sigma_1 \\ \Sigma_2 \\ \Sigma_3 \end{Bmatrix} &= \frac{2}{3} \Sigma_{\mathrm{eq}}^{\mathrm{vm}} \begin{Bmatrix} \cos\theta \\ \cos\left(\theta - \frac{2\pi}{3}\right) \\ \cos\left(\theta + \frac{2\pi}{3}\right) \end{Bmatrix} + \Sigma_{\mathrm{h}} \begin{Bmatrix} 1 \\ 1 \\ 1 \end{Bmatrix} \\
&= \Sigma_{\mathrm{eq}}^{\mathrm{vm}} \left(\frac{2}{3} \begin{Bmatrix} \cos\theta \\ \cos\left(\theta - \frac{2\pi}{3}\right) \\ \cos\left(\theta + \frac{2\pi}{3}\right) \end{Bmatrix} + T \begin{Bmatrix} 1 \\ 1 \\ 1 \end{Bmatrix} \right)
\end{aligned}
\tag{12}
$$

In this relation, Σ_{h} is the hydrostatic stress and T the stress triaxiality, defined by

$$
T = \frac{\Sigma_{\mathrm{h}}}{\Sigma_{\mathrm{eq}}^{\mathrm{vm}}}
\tag{13}
$$

and the deviatoric angle is in the range $\theta \in [0, 2\pi\rangle$. The expressions for the principal stress components in Equation (12) will prove useful in the finite element procedure. Since the ratios between different principal stress components reduce to functions of only θ and T, we may discern and impose stress states in a simple and concise manner.

With reference to Equation (12), we now understand that by defining the deviatoric angle and the stress triaxiality, the ratios between the principal stress components are uniquely defined. Following the procedure introduced by Faleskog et al. (1998) for plane strain situations and further extended by Kim et al. (2004) to account for three-dimensional stress states, we introduce normalized principal stress ratios on the form

$$
\psi_1 = \frac{\Sigma_1}{\Sigma_{\mathrm{max}}}, \quad \psi_2 = \frac{\Sigma_2}{\Sigma_{\mathrm{max}}}, \quad \psi_3 = \frac{\Sigma_3}{\Sigma_{\mathrm{max}}}
\tag{14}
$$

where Σ_i are the macroscopic principal stress components applied to the unit cell edges, and $\Sigma_{\mathrm{max}} = \max\left(\Sigma_1, \Sigma_2, \Sigma_3\right)$. Thus, the principal stress ratios are always restricted by $\psi_i \leq 1$, and uniquely defined by a set of parameters (T, θ) such
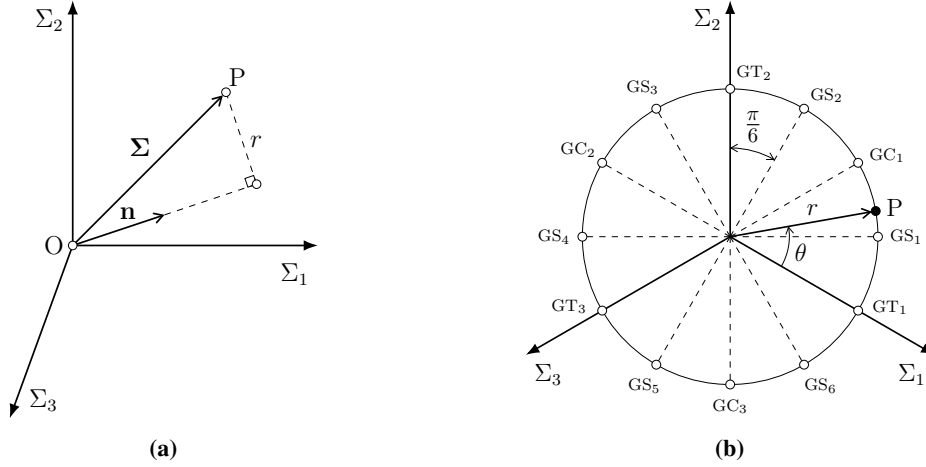
Figure 3: Schematic of the macroscopic stress state. Figure (a) shows the stress state P in the principal stress space with the hydrostatic axis $\mathbf{n}$ and radius r in the deviatoric plane indicated. Figure (b) shows the same stress state along with the investigated stress states for any given stress triaxiality T in the deviatoric plane. GT_i, GS_i, and GC_i indicate successive states of generalized tension, shear, and compression, respectively.

that we may write

$$\psi_i = \psi_i(T, \theta) \tag{15}$$

These stress ratios are the only quantities needed for the nonlinear kinematic constraints that are used to enforce proportional loading to the unit cell. These kinematic constraints were imposed to the FE model by using the multi-point constraint (MPC) subroutine in ABAQUS/Standard. Details regarding the kinematic constraints are provided in Appendix B.1. We also note that expositions of the MPC procedure are given by Faleskog et al. (1998), Kim et al. (2004), Barsoum and Faleskog (2007), Cheng and Guo (2007), Vadillo and Fernández-Sáez (2009), Wong and Guo (2015), Liu et al. (2016), and Dæhli et al. (2016a), and the reader is advised to consult these references for further details.

3.3. Applied range of macroscopic stress states

In order to investigate various positions on the yield surface systematically, we span the deviatoric stress plane with increments of the deviatoric angle equal to $\Delta\theta = 30°$. In addition, four different stress triaxiality levels are imposed for each deviatoric stress state to elucidate effects of the hydrostatic stress. These correspond to $T = 2/3$, 1, 5/3, and 3, thus encompassing stress states ranging from plane stress biaxial tension to highly constrained problems, such as in front of crack tips. The imposed deviatoric stress states are shown in Figure 3b and summarized in Table 2 where GT_i, GC_i, and GS_i denote successive states of generalized tension, compression, and shear, respectively. We note that also the Lode parameter L appears in this table, which is defined on the form

$$L = \frac{2\Sigma_{II} - \Sigma_I - \Sigma_{III}}{\Sigma_I - \Sigma_{III}} \tag{16}$$

where $\Sigma_I \geq \Sigma_{II} \geq \Sigma_{III}$ are the ordered principal stress components.

For isotropic materials, there is no need to distinguish between successive generalized stress states, for instance GT_1, GT_2, and GT_3, due to the six-fold symmetry of the yield surface. In the case of plastically anisotropic materials, however, the yield surface does not possess this symmetry. As perceived from Figures 1a-1e, the radius of the yield surface is greatly dependent upon the position in the deviatoric plane. Consequently, the orientation of the ordered principal stress directions with respect to the material axes is decisive for the magnitude of the stress state and the resulting plastic flow. To reflect this in the unit cell simulations, we have aligned the material axes $\mathbf{m}_i$ with the macroscopic Σ_i-axes, as shown in Figure 2a. This means that the ordered macroscopic principal stress directions will be oriented along different material axes depending upon the deviatoric angle θ imposed in the calculation.

9

Table 2: Deviatoric stress states in terms of the deviatoric angle and the Lode parameter.

Stress state	Deviatoric angle	L
GT_1	0°	−1
GS_1	30°	0
GC_1	60°	1
GS_2	90°	0
GT_2	120°	−1
GS_3	150°	0
GC_2	180°	1
GS_4	210°	0
GT_3	240°	−1
GS_5	270°	0
GC_3	300°	1
GS_6	330°	0

3.4. Unit cell results

Owing to the large number of stress states investigated for each generic texture, a total of $12 \cdot 4 \cdot 6 = 288$ unit cell calculations have been conducted. Hence, the resulting amount of data is quite extensive and most of it will not be presented in this paper. The large number of computations also made it necessary to restrict the number of unit cell configurations. Hence, we have neither accounted for the effects of initially non-spherical void shapes and non-uniform spatial void distributions, nor the influence of initial void volume fraction. Such effects have been documented previously in the literature for plastically anisotropic materials, see for example Keralavarma and Benzerga (2010) or Keralavarma et al. (2011) in the case of axisymmetric unit cells governed by the Hill anisotropic yield criterion (Hill, 1948). The influence of matrix anisotropy and non-quadratic yield surfaces are thus the only effects that are explicitly accounted for in the current work.

For the purpose of displaying various mechanical response parameters against the global deformation, we use a von Mises strain norm as a macroscopic equivalent strain measure throughout the remainder of this paper. The equivalent global strain is then calculated from

$$E_{\text{eq}}^{\text{vm}} = \sqrt{\frac{2}{3}\mathbf{E}' : \mathbf{E}'} \tag{17}$$

where $\mathbf{E}'$ is the deviatoric logarithmic strain tensor on the macroscopic level.

Figures 4a-4f present snapshots of the unit cell at the first frame extracted from the analyses after the onset of material softening. The spatial distribution of the accumulated plastic strain p in the matrix, as calculated from Equation (8), is plotted on the deformed configurations. Only configurations pertaining to a triaxiality $T = 2/3$ and a deviatoric angle of $\theta = 0°$, meaning uniaxial tension along $\mathbf{m}_1$ with a superposed hydrostatic stress, are shown. The corresponding curves for the equivalent stress-strain response and the void growth slightly beyond the peak stress are shown in Figure 5, thus only indicating the void growth phase.

3.4.1. Spatial distribution of plastic strain

The distribution of the accumulated plastic strain throughout the unit cell is markedly different between the various matrix descriptions, as seen from Figure 4. This is of interest because inspection of the fringe plots in Figure 4 and the rate of void growth in Figure 5 reveals that the ability to distribute plastic strain greatly influences the void growth. In the unit cell simulations where the accumulated plastic strain is more evenly distributed, for instance the brass texture, the void growth rate is decreased and the voids tend to become more elongated in the main loading direction. Thus, evenly distributed plastic strain fields lead to slower void growth. This is analogous to the case of necking in tensile bars, where greater ability to distribute plastic strains is known to cause more diffuse necking and higher ductility (Pardoen, 2006). This effect is closely connected to a reduced stress triaxiality locally in the neck with more distributed plastic deformation. In the unit cell analogue, this reduces the stress triaxiality in the ligament between adjacent voids.
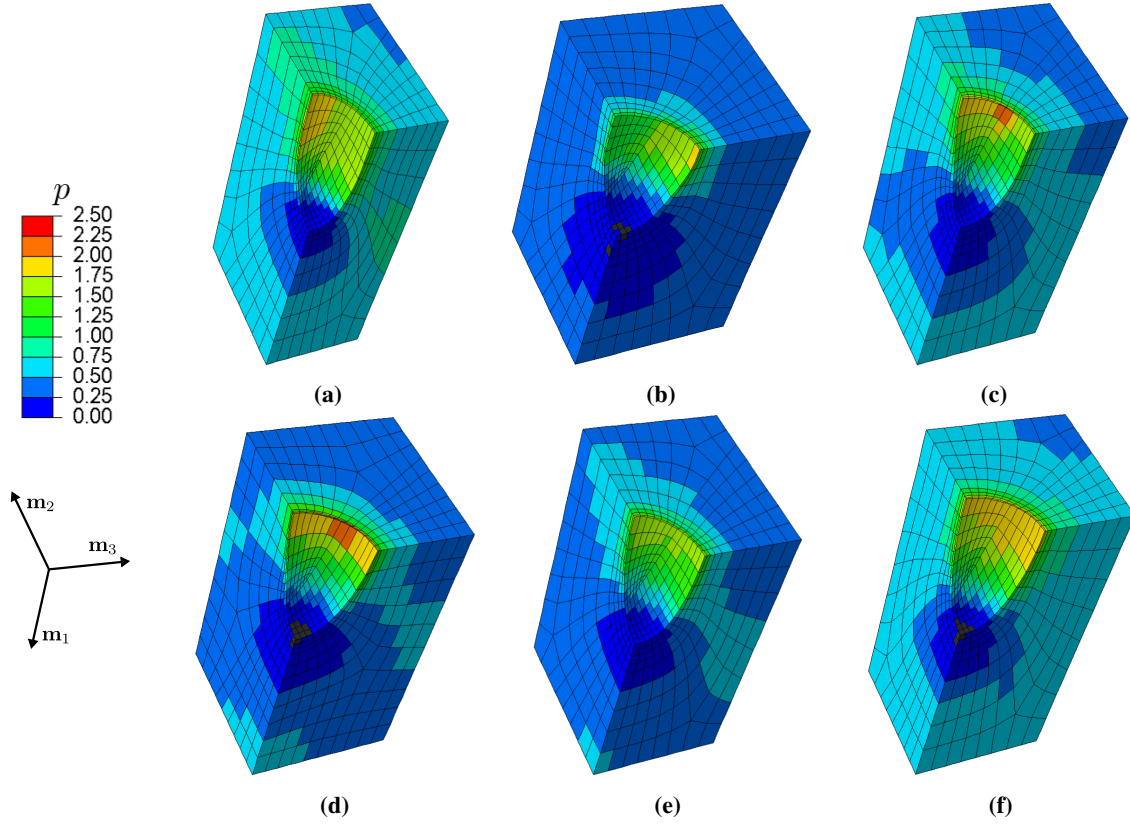
Figure 4: Deformed configurations with fringes of matrix accumulated plastic strain for all six textures in the case of an applied external loading corresponding to $T = 2/3$ and $\theta = 0°$. The snapshots of the deformation are taken at the first frame extracted after the onset of material softening. The subfigures correspond to (a) brass, (b) copper, (c) cube, (d) Goss, (e) S, and (f) random textures, respectively.

The question then remains what causes the differences observed in the spatial strain distribution between the textures. The external loading state is similar for all the shown unit cells, corresponding to generalized tension along $\mathbf{m}_1$ with $T = 2/3$. Moreover, the strain hardening of the matrix is identical and on the form written in Equation (7), and since we are considering loading along the reference direction, meaning $\sigma_{\text{eq}}^{\text{vm}} = \sigma_{\text{M}}$, the equivalent stress at yielding is the same for all materials under the given global loading condition. This implies some correlation between the plastic anisotropy, or more specifically the plastic flow direction, and the observed differences in the spatial distribution of the accumulated plastic strain.

First, note that the void is the single source of heterogeneity in the mechanical field quantities. Due to this heterogeneity, there will be an interplay between geometric effects due to the discrete void and the plastic anisotropy of the matrix. The global deformation, dictated by the plastic anisotropy through the associated flow rule, represents a significant constraint to the void shape that develops during the course of the deformation. In the general case, the plastic flow of the material leads to different global deformation along the material axes, meaning that the current unit cell lengths l_i are not equal ($l_1 \neq l_2 \neq l_3$). With reference to Figure 4, even in the case of generalized tension with $\mathbf{m}_1$ as the major loading direction, the unit cell edges may not undergo identical displacement along $\mathbf{m}_2$ and $\mathbf{m}_3$, which means that $l_2 \neq l_3$, due to the anisotropic plastic flow. This has major implications for the resulting void shape, which can differ quite substantially depending on the texture (see Section 3.4.2), and will lead to differences in the spatial field quantities in the proximity of the void. Close to the void surface, the material elements tend to rotate which induces shear stresses and strains, and thus impose locally non-proportional stress paths. The stress components, and thus the plastic strain rate components via Equation (6), depend greatly upon the anisotropy coefficients entering the linear
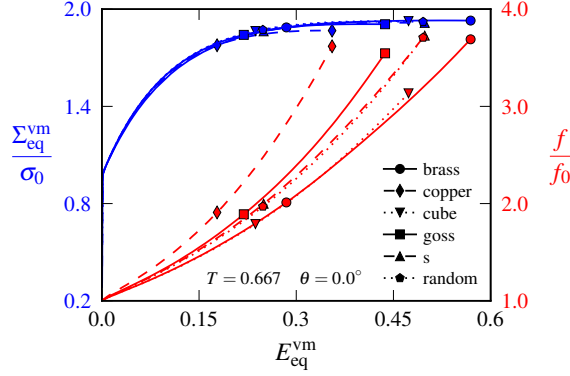
11

Figure 5: Stress-strain response and void growth for all the analysed textures under external loading defined by $T = 2/3$ and $\theta = 0°$

transformation tensors $\hat{\mathbf{A}}^{(1)}$ and $\hat{\mathbf{A}}^{(2)}$ in Equation (3), which are texture dependent. In turn, this causes differences in the plastic flow and further in the accumulated plastic strain field in the same region. These effects emerge in the vicinity of the void surface while the global deformation is still rather small, and spread towards the external boundaries during continued deformation.

3.4.2. Void shape evolution

The void aspect ratios (w_i) are plotted in Figures 6 and 7 against the macroscopic equivalent strain slightly beyond the peak stress. The figures correspond to triaxialities of $T = 1$ and $T = 3$, respectively, to be able to discern results pertaining to moderate and high stress triaxialities. Only states of generalized tension ($\theta = 0°, 120°, 240°$) are shown, for the purpose of enhancing the readability of the plots, but these loading conditions suffice to demonstrate effects of material orientation on the resulting evolution of the void shape. The void aspect ratios are taken on the form

$$w_{\text{II}} = \frac{R_{\text{II}}}{R_{\text{I}}}, \quad w_{\text{III}} = \frac{R_{\text{III}}}{R_{\text{I}}} \tag{18}$$

where subscripts I, II, and III refer to the ordered principal stress directions. Thus, these ratios are always calculated with respect to the void radius in the direction of the global maximum stress Σ_{I}. This means that for instance when $\theta = 0°$, where $\Sigma_{\text{I}} = \Sigma_1, \Sigma_{\text{II}} = \Sigma_2 = \Sigma_3 = \Sigma_{\text{III}}$, we have $w_{\text{II}} = R_2/R_1$ and $w_{\text{III}} = R_3/R_1$.

From the plots presented in Figures 6 and 7, and from the deformed unit cell configurations in Figure 4, we readily observe that the matrix anisotropy has a pronounced effect on the resulting void shape evolution. The direction of the macroscopic plastic strain rate, uniquely linked to the macroscopic stress state through the associated flow rule, seems highly important in that regard. If the elastic deformations are negligible compared to their plastic counterparts, the global displacement of the unit cell edges is dictated by the direction of plastic flow, at least in the range of moderate void growth and prior to the onset of coalescence. Due to the assumption of associated flow, the plastic rate-of-deformation is then co-directional with the gradient to the yield surface. With reference to the yield surfaces shown in Figure 1, this means that in situations where the normal to the yield surface is collinear to one of the σ_i-axes, the unit cell boundaries tend to deform similarly along the two other coordinate axes $\mathbf{m}_{j \neq i}$. This promotes a spheroidal void evolution, either in terms of an oblate or a prolate shape depending upon the deviatoric angle, stress triaxiality, and the material orientation. By considering Figures 6 and 7, such observations can be made for the cube texture in loading case GT$_3$ ($\theta = 240°$) and the S texture for GT$_2$ ($\theta = 120°$). We also observe the same tendency for the Goss texture in loading case GT$_1$ ($\theta = 0°$) when $T = 1$. For the random texture, this occurs for all states of generalized tension and compression (GT$_i$ and GC$_i$), as demonstrated for the generalized tension states in Figures 6f and 7f. This demonstrates the isotropic properties of the random texture anticipated in the presentation of the matrix materials in Section 2.

Another noteworthy evidence for the coupling between the yield surface and the void shape evolution (through the global unit cell deformation) can be deduced from Figure 6. For instance, the void aspect ratios w_{II} and w_{III} for the Goss texture are respectively identical for GT$_2$ ($\theta = 120°$) and GT$_3$ ($\theta = 240°$), such that $w_{\text{II}}^{\text{GT}_2} = w_{\text{II}}^{\text{GT}_3}$ and $w_{\text{II}}^{\text{GT}_2} = w_{\text{III}}^{\text{GT}_3}$. From the yield surfaces presented in Figure 1, we find that these stress states possess some form of symmetry in terms

of the plastic flow direction. If we order the components of the yield surface normal as it appears in the deviatoric stress plane, they are identical for the two stress states, however pointing along different material axes $\mathbf{m}_i$. In terms of the unit cell deformation, this implies that the global deformation of the unit cell is identical, but rotated relative to the fixed global coordinate system x_i. Similar observations are made for the copper texture for the same loading states, and also to some extent for the S texture in the case of GT_1 ($\theta = 0°$) and GT_3 ($\theta = 240°$). For the random texture, all states of generalized tension and compression comply with this observation due to its isotropic properties leading to six-fold symmetry of the yield surface.

The numerical data shown in Figure 7 pertain to a stress triaxiality of $T = 3$. These unit cell results show that as the external hydrostatic tension is increased, the void shape evolution is less pronounced. This is indicated by w_i being closer to unity in most loading cases. However, the voids tend to evolve into an oblate form rather than the prolate form taken under lower traxialities (see Figure 6) for the given deviatoric loading conditions. We also notice that the principal void radii are more similar for the different loading states displayed in the figure, which is seen by comparing the curves in Figures 6 and 7. Consequently, an increased triaxiality diminishes effects of the deviatoric angle, or equivalently the Lode parameter. Moreover, differences in the void aspect ratio curves between the various matrix descriptions are less pronounced. This observation suggests that as the stress triaxiality is increased, the underlying matrix anisotropy, and thus the directional dependency, has less influence on the resulting void growth and the problem is mainly governed by spherical void expansion.

3.4.3. Void growth

Examination of the numerical data for the void growth in Figures 8-10 indicates a strong correlation between the stress state and the void growth rate. Not only is there a noticeable difference between states of generalized tension, compression, and shear, but also between successive states of the same kind. Figure 8 reveals that the latter is purely related to the matrix anisotropy, since the stress states GT_1 ($\theta = 0°$) and GT_2 ($\theta = 120°$), GC_1 ($\theta = 60°$) and GC_2 ($\theta = 180°$), and GS_1 ($\theta = 30°$) and GS_2 ($\theta = 90°$) mutually yield the same response for the random texture. By comparing the void growth curves in Figures 8-10 to the yield surfaces plotted in Figure 1 we may also detect another interesting effect. In general, the unit cell simulations demonstrate that a larger radius of the yield surface, as it appears in the deviatoric plane, results in more rapid growth of the voids. This is readily observed for instance in the case of the brass texture in which the most rapid void growth is obtained for $\theta = 120°$ while the slowest void growth corresponds to $\theta = 30°$. These positions on the yield surface are seen to coincide with the largest and smallest radius, respectively. The situation is similar for the cube texture, but not as apparent because the yield surface is more rounded for that texture.

Shinohara et al. (2016) argue that the difference in the void growth rate obtained in different loading directions is a mere effect of the stress triaxiality definition, which does not account for the equivalent stress measure used. They further demonstrate that using a triaxiality definition consistent with the equivalent stress measure gives approximately the same void growth along the different material axes in the loading scenarios presented in their work. This seems like a plausible explanation for the observed differences, since keeping a constant stress triaxiality externally indeed means that the imposed hydrostatic stress is different. From Equation (13), we have that

$$\Sigma_{\mathrm{h}} = T\Sigma_{\mathrm{eq}}^{\mathrm{vm}} = \sqrt{\frac{3}{2}}Tr \tag{19}$$

We then readily see that changing r will affect Σ_{h} when T is kept constant. Further investigation of this matter has not been attempted in this work, but the authors have addressed this issue in currently unpublished work dealing with non-quadratic isotropic yield surfaces. We found that using a stress triaxiality in line with the adopted equivalent stress measure

$$T^* = \frac{\Sigma_{\mathrm{h}}}{\Sigma_{\mathrm{eq}}} = T\frac{\Sigma_{\mathrm{eq}}^{\mathrm{vm}}}{\Sigma_{\mathrm{eq}}} \tag{20}$$

had some effects on the void growth rate, but was not sufficient to account for the rather large difference in the porosity evolution between the quadratic and the non-quadratic matrix description.

It is now a well-established fact that the Lode parameter affects the void growth, see for instance Zhang et al. (2001) or Kim et al. (2004), which is also observed in our simulations. Evidence for this matter is provided by the curves for GT_1 ($\theta = 0°$) and GC_2 ($\theta = 180°$) for all three textures displayed in Figures 8-10. The first stress state represents a generalized tension loading while the latter represents generalized compression. Under these loading conditions, the
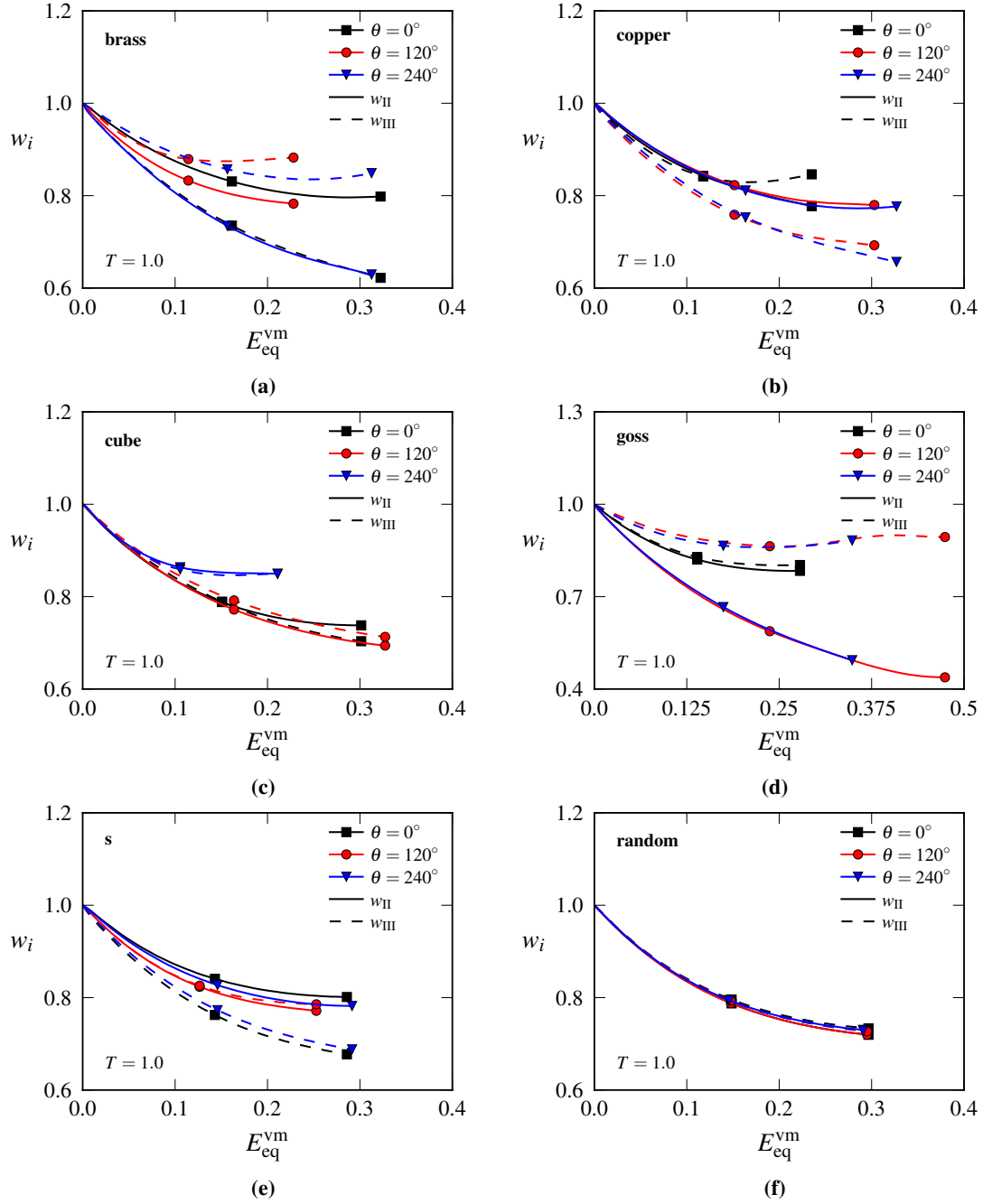
13

Figure 6: Evolution of the void shape for $T = 1$. The ratio between the principal void radii w_i are plotted against the equivalent von Mises strain for (a) brass, (b) copper, (c) cube, (d) Goss, (e) S, and (f) random textures, respectively. A few data points beyond the onset of material softening are included in the plots.
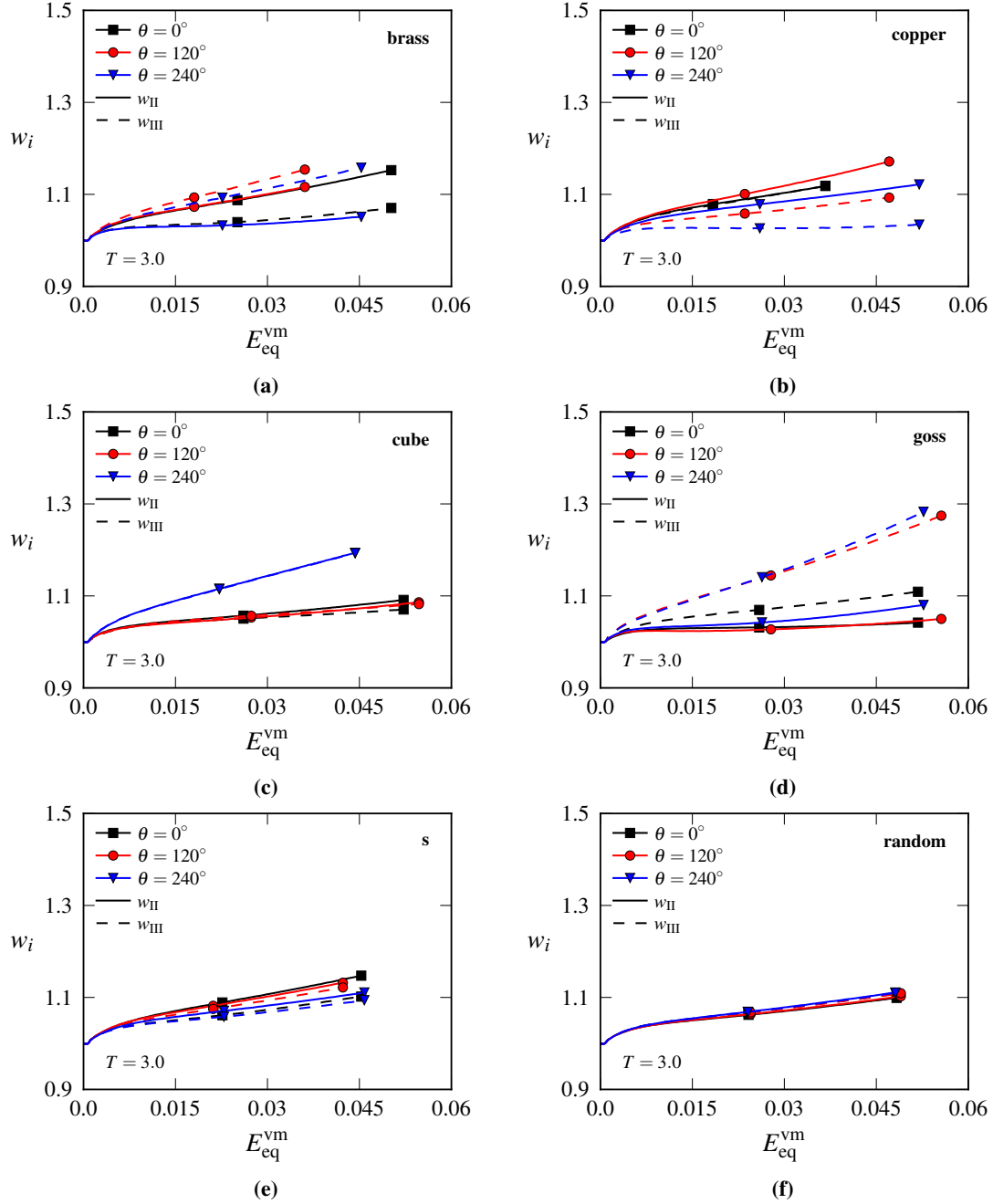
14

Figure 7: Evolution of the void shape for $T = 3$. The ratio between the principal void radii w_i are plotted against the equivalent von Mises strain for (a) brass, (b) copper, (c) cube, (d) Goss, (e) S, and (f) random textures, respectively. A few data points beyond the onset of material softening are included in the plots.

radius is identical since we do not discern between the yield stress in compression and tension. In agreement with established literature, we find that void growth is more rapid in generalized tension provided the yield stress is similar. This effect is not caused by the matrix anisotropy. However, the matrix anisotropy clearly has an influence on this Lode effect, since it is readily perceived that the difference in void growth rate is much more prominent for both the random and brass textures than for the cube texture in the aforementioned stress states.
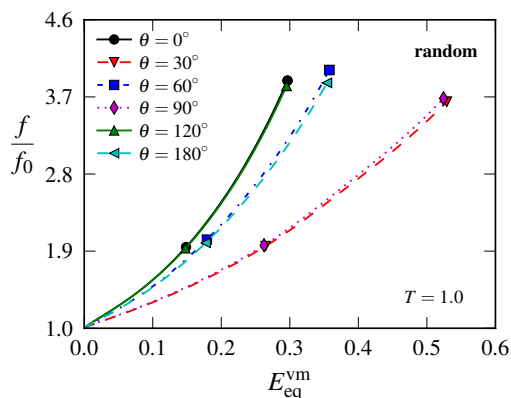
Figure 8: Evolution of the void volume fraction for the random texture for a number of different deviatoric angles. The stress triaxiality was $T = 1.0$ for these curves.
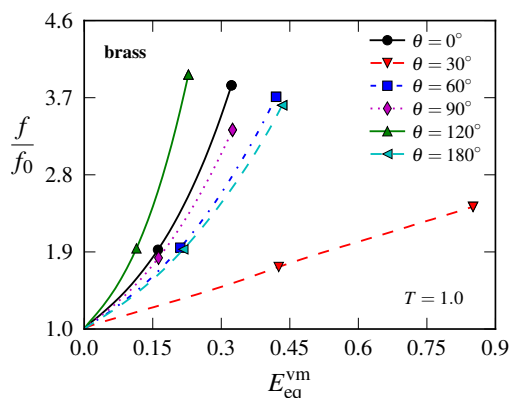
Figure 9: Evolution of the void volume fraction for the brass texture for a number of different deviatoric angles. The stress triaxiality was $T = 1.0$ for these curves.

Not only the radius of the yield surface affects the resulting void growth rate. Also the normal to the yield surface has an effect, due to the associated flow rule adopted herein. Cross-examination of the void growth curves for the random, brass, and cube textures for loading state GT_1 ($\theta = 0°$) demonstrates that even for the same deviatoric angle and radius of the yield surface there are differences in the rate of void expansion. Similar observations can be made for curves corresponding to GC_2 ($\theta = 180°$). Since, in these cases, the only difference in the macroscopic boundary conditions is the plastic flow direction, this indicates an important effect with respect to the direction of the plastic strain rate, which is obviously dictated by the plastic anisotropy. This was also addressed to some extent in the discussion of the void radii in the preceding section.

Although the unit cell calculations reveal effects of both the yield surface radius and the plastic flow direction on the void growth, the growth rate cannot be exclusively linked to these two sources of influence. This is most easily demonstrated for loading conditions with the same Lode parameter. Considering for instance the loading states GS_1 ($\theta = 30°$) and GS_2 ($\theta = 90°$) in Figure 10, for which the Lode parameter is $L = 0$, we readily observe that the void growth rate is different in these two cases. But from the yield surfaces in Figure 1, we find that the radius and the plastic
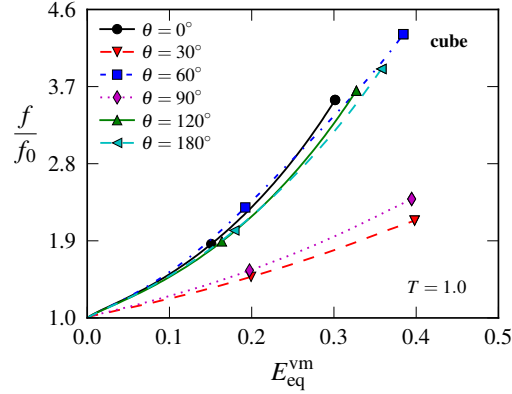
Figure 10: Evolution of the void volume fraction for the cube texture for a number of different deviatoric angles. The stress triaxiality was $T = 1.0$ for these curves.

flow direction are respectively identical, however oriented along different global coordinate axes. This bears evidence for another source of discrepancy, which is not linked to the macroscopically imposed boundary conditions but rather to the heterogeneity of the field variables. The implication is that local fluctuations in the mechanical quantities around the void cause large differences as the plastic deformation progresses. As discussed in Section 3.4.1, this is an effect of the heterogeneity imposed by the void geometry leading to rotation and shearing of the elements close to the void surface. The induced element shearing is especially important because, as a consequence, this causes shear stresses and generally non-proportional loading paths in the proximity of the void. The influence of shear stress components on the resulting yield surface is not accounted for in Figure 1, since these are generated under the assumption that the material is loaded by normal stress components along the material axes. By inducing shear strains, different components in the linear transformation tensors $\hat{\mathbf{A}}^{(i)}$ are invoked which are generally not identical. Keeping in mind that the material axes are kept fixed and we rather rotate the loading axes, we note that varying the principal loading directions globally induces different shear stress components in the proximity of the void. Evidently, this causes differences in the plastic strain field surrounding the void which ultimately affects the void growth rate. We also note that the simplified calibration process of the anisotropy parameters from plane stress FC Taylor calculations (see Section 2.2) can potentially influence the local stress values in regions of pronounced shear deformations.

4. Porous plasticity model

The material response at the intermediate scale, as represented by unit cell models, must be homogenized using a constitutive relation in order to be suitable for large scale applications. Different homogenization approaches may be utilized to suit this purpose. Due to the complexity associated with deriving a closed-form yield criterion for the underlying matrix plasticity formulation, we will in the following propose a heuristic extension of the Gurson model. The model is thus founded on a micromechanical basis, however without the calculation of an upper-bound plastic limit. We have also previously examined the predictive capabilities of this porous plasticity model for the cube and Goss textures (Dæhli et al., 2016b).

4.1. Model formulation

Following along the same lines as in for example Doege and Seibert (1995), Steglich et al. (2010), and Shinohara et al. (2016), we propose a heuristic extension of the Gurson-Tvergaard model (Gurson, 1977; Tvergaard, 1981) to account for plastic anisotropy of the matrix material

$$\Phi\left(\hat{\boldsymbol{\Sigma}}, \sigma_{\mathrm{M}}, f\right) = \left(\frac{\Sigma_{\mathrm{eq}}}{\sigma_{\mathrm{M}}}\right)^2 + 2q_1 f \cosh\left(q_2 \frac{3\Sigma_{\mathrm{h}}}{2\sigma_{\mathrm{M}}}\right) - 1 - (q_1 f)^2 \leq 0 \tag{21}$$

17

Here, $\Phi\left(\hat{\boldsymbol{\Sigma}}, \sigma_{\mathrm{M}}, f\right)$ denotes the macroscopic yield function defining the periphery and interior of the elastic domain, σ_{M} is the matrix flow stress governed by Equation (7), Σ_{h} is the macroscopic hydrostatic stress, f is the void volume fraction, and q_i are the model parameters introduced by Tvergaard (1981). However, Σ_{eq} is now the macroscopic equivalent stress given by Equation (4), being consistent with the Barlat Yld2004-18p model, which accounts for the plastic anisotropy of the matrix material. The associated flow rule is invoked, such that

$$\hat{\mathbf{D}}^{\mathrm{p}} = \dot{\Lambda}\frac{\partial\Phi}{\partial\hat{\boldsymbol{\Sigma}}} \tag{22}$$

where $\dot{\Lambda}$ is recognized as the plastic parameter.

As for the unit cell model, the work hardening of the matrix material is governed by the one-term Voce law shown in Equation (7) with the material parameters listed in Table 1. The matrix accumulated plastic strain rate is then related to the plastic dissipation through

$$\dot{p} = \frac{\hat{\boldsymbol{\Sigma}} : \hat{\mathbf{D}}^{\mathrm{p}}}{(1-f)\,\sigma_{\mathrm{M}}} \tag{23}$$

The elastic response is governed by a hypoelastic formulation using the generalized Hooke's law on the same form as presented in Equation (2). Thus, a linear relationship is assumed between the macroscopic stress rate and the macroscopic elastic rate-of-deformation. This implies that any influence of the porosity on the elastic properties is neglected, in accord with the assumption made by Gurson (1977). Such an approximation is deemed appropriate in the case of small porosities, which is usually the case for applications dealing with metal alloys.

The last part of the constitutive framework consists in defining the evolution of the void volume fraction. Plastic incompressibility of the matrix material gives

$$\dot{f} = (1-f)\,\mathrm{tr}(\hat{\mathbf{D}}^{\mathrm{p}}) \tag{24}$$

for the evolution of the void volume fraction. Some effects of the plastic anisotropy are expected to be captured by this expression, since the volumetric plastic strain rate implicitly depends upon the anisotropy through the associated flow rule. However, this evolution law does not incorporate void shape effects, being a direct result of the assumptions made in deriving the Gurson yield potential. Such effects might be significant due to the directional dependency of the matrix material and the interplay between the two sources of anisotropy, as also indicated by the unit cell results presented in Section 3.4. A heuristic way of including such void shape effects might be to directly incorporate a void shape correction term in Equation (24) without changing the yield function in Equation (21). We have not made any attempt towards this in the present work.

As for the matrix material presented in Section 2, we used a UMAT subroutine based on a semi-implicit integration scheme for the temporal integration of the rate constitutive equations (Belytschko et al., 2000). Substepping was employed in which allowable strain increments provided to the user subroutine were limited to $\Delta\bar{\varepsilon} = \Delta t\,\sqrt{\hat{\mathbf{D}} : \hat{\mathbf{D}}} \leq 0.05\sigma_0/E$, where the total rate-of-deformation is used to account for the volumetric strain. More details on the substepping have been provided in Section 2.1.

Before proceeding to the next section, we should note that the q_i parameters are used to tune the response of the porous plasticity model through an optimization process. Thus, effects of plastic anisotropy are partly accounted for by the equivalent stress formulation, and partly by the q_i parameters which will depend upon the anisotropy of the matrix. These parameters are presumed to enhance the predictions in the intermediate range of the stress triaxiality values. We note that the porous plasticity model was implemented using a corotational formulation. However, in the present context it does not affect the calculations since normal stress components are imposed along the material axes of a single material point.

4.2. Imposed stress states

Homogeneous boundary conditions in line with those applied in the unit cell calculations are imposed to the porous plasticity model. Since the porous plasticity model governs the homogenized response of the aggregate material, these boundary conditions may be applied directly in terms of the strain increments that are fed to the material subroutine. To conform to the unit cell simulations, it is then necessary to evaluate appropriate strain increments such that the stress triaxiality T and the deviatoric angle θ are maintained to the values listed in Table 2. Thus, we impose the ratio

between principal stress components $\psi_i(T, \theta)$ and update the strain increments accordingly. This is realized using an approach that closely resembles the method in Nahshon and Hutchinson (2008) to prescribe the deformation outside an imperfection band in localization analyses, however modified to accommodate use of the entire deviatoric stress plane. Details of this procedure are given in Appendix B.2.

4.3. Calibration of the porous plasticity model

An important part of the present study is to examine the predictive capabilities of the proposed porous plasticity model for the generic textures used herein. Assuming that the unit cell model outlined in Section 3 gives an adequate representation of the aggregate material at the microstructural level, we further use the numerical data from the unit cell calculations as reference curves to calibrate the porous plasticity model. To this end, we employed a sequential least-square optimization procedure provided by the SLSQP minimization solver of the Scipy Python package. For details regarding this numerical tool, the reader is advised to consult the reference manual of Scipy (2016).

We introduce two residuals (e_Σ and e_f) that are used to define the cost function for the optimization. These residuals are taken as strain-weighted averages of the difference between the unit cell (UC) and the porous plasticity model (PPM) on the form

$$e_\Sigma = \frac{1}{N_{ss}} \sum_{i=1}^{N_{ss}} \frac{\int_0^{E_{eq}^{max}} |\Sigma_{eq}^{PPM} - \Sigma_{eq}^{UC}|_i \, dE_{eq}}{\int_0^{E_{eq}^{max}} \frac{1}{2} \left(\Sigma_{eq}^{PPM} + \Sigma_{eq}^{UC}\right)_i \, dE_{eq}} \tag{25a}$$

$$e_f = \frac{1}{N_{ss}} \sum_{i=1}^{N_{ss}} \frac{\int_0^{E_{eq}^{max}} |f^{PPM} - f^{UC}|_i \, dE_{eq}}{\int_0^{E_{eq}^{max}} \frac{1}{2} \left(f^{PPM} + f^{UC}\right)_i \, dE_{eq}} \tag{25b}$$

Here, N_{ss} indicates the total number of stress states, the magnitude of a quantity x is denoted $|x|$, and the equivalent strain is given by Equation (17). All the stress states for a given texture ($N_{ss} = 48$) were used to calculate the residuals. In the computations, we defined the limit of the definite integrals as the equivalent strain slightly beyond the maximum stress from the respective unit cell analyses $E_{eq}^{max} \approx E_{eq}^{UC}\left(\Sigma_{eq}^{vm} = 0\right)$. Thus, we account for the void growth phase and incipient material softening in the calibration of the porous plasticity model, but we exclude numerical data suffering from mesh distortion due to the large deformations emerging locally in the unit cell analyses.

The cost function is defined by

$$e = w_\Sigma e_\Sigma + w_f e_f = w_\Sigma e_\Sigma + (1 - w_\Sigma) e_f \tag{26}$$

with $w_\Sigma \in [0, 1]$ in the optimization process. The residuals were given equal weight $w_\Sigma = w_f = 1/2$ herein, since the calibrated constants q_i were only slightly affected by the residual weights. This is presumably due to the inherent coupling between the rate of void growth and the macroscopic stress state through the associated flow rule. A tolerance of $\Delta e \leq 10^{-7}$ for the difference in the cost function between two iterations was used to terminate the optimization process. Figures 11a-11f show the difference between the porous plasticity model and the unit cell results as a density plot for a range of q_1 and q_2 parameters. These results demonstrate that a large set of q_i parameters can be used that result in nearly the same correspondence to the unit cell data, indicated by the blue tinted band in the error density plots. As such, the optimization procedure is not trivial since there exist a large number of local minima, and a global minimum is not likely to be found in the optimization process. The optimized values found from the calibration procedure are listed in Table 3 and shown as a red dot in Figures 11a-11f. We note that the q_i values for the Goss texture violates the Hashin-Shtrikman bounds (Hashin and Shtrikman, 1963), which according to Leblond et al. (1994) are met when $q_1 \geq 4/3$. However, parameter sets lying within the Hashin-Shtrikman bounds can readily be found without compromising the accuracy of the porous plasticity model, as perceived from the error density plots in Figure 11. We lastly mention that the error estimates e_Σ, e_f, and e from the last increment in the optimization are listed in Table 3. These values unanimously show that the resulting error for the porosity is much greater than that for the equivalent stress. The total error e is relatively similar for all the considered textures.

Figure 12 shows the initial yield loci for the brass texture using the calibrated material constants q_i. Figure 12a pertains to generalized axisymmetric stress states, while Figure 12b shows surfaces for the generalized shear states. We readily observe the effect of anisotropy in the model, indicated by the shift of the yield curves for the different
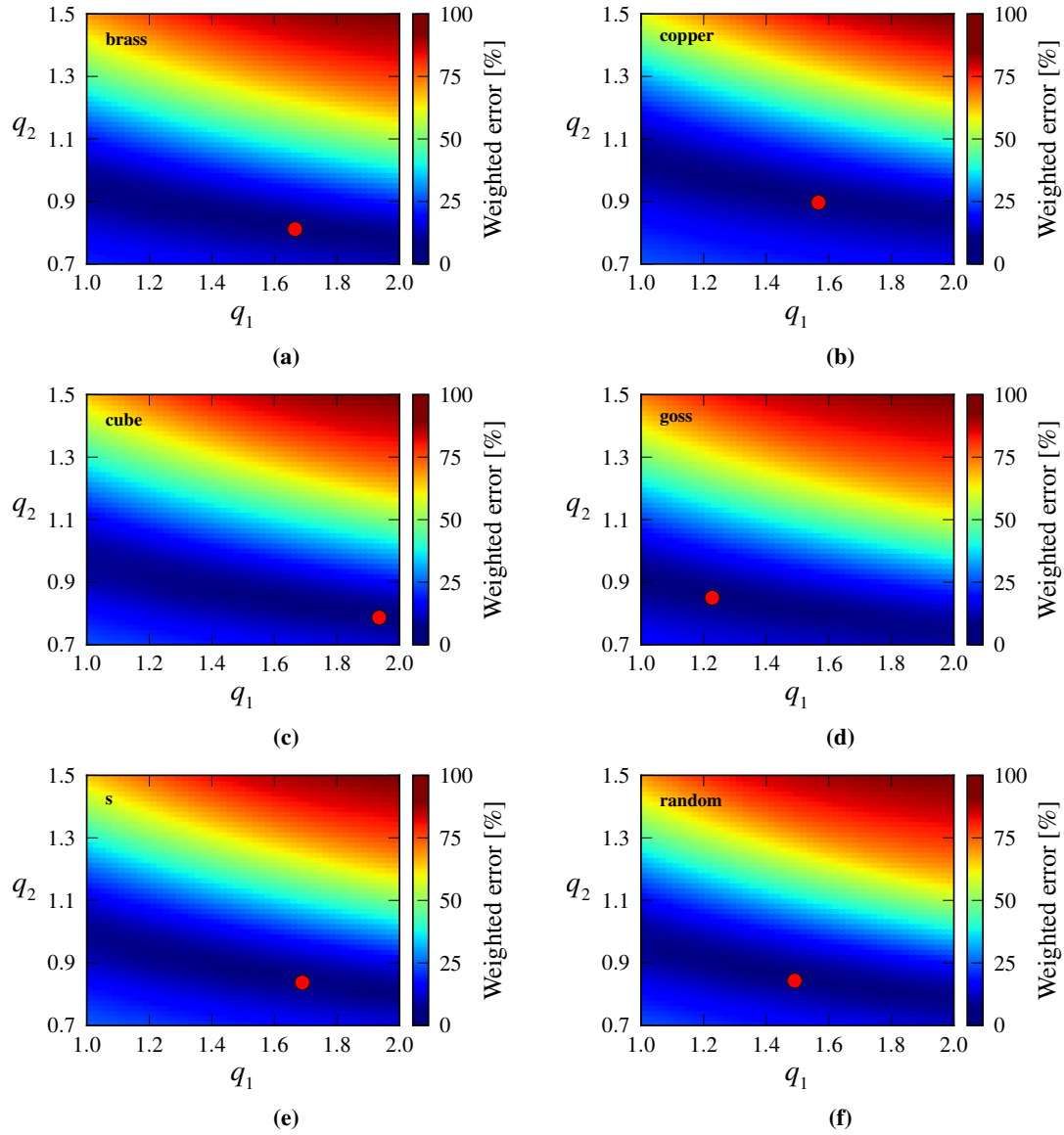
Figure 11: Density plot of the error estimates obtained by comparing the PPM model predictions to the unit cell response. The individual plots correspond to the (a) brass, (b) copper, (c) cube, (d) Goss, (e) S, and (f) random textures. Blue colour indicates a comparatively small error while red colour indicates a rather large error. The red dot indicates the q_i parameters obtained from the optimization procedure.

Table 3: List of the porous plasticity parameters q_i that were found in the optimization procedure. The residuals e_Σ, e_f, and e obtained in the last increment of the optimization are given.

Matrix	Brass	Copper	Cube	Goss	S	Random
q_1	1.666	1.567	1.935	1.227	1.689	1.491
q_2	0.812	0.897	0.787	0.850	0.837	0.843
e_Σ [%]	0.710	0.789	0.659	0.814	0.594	0.637
e_f [%]	8.401	9.710	6.519	7.826	6.198	6.617
e [%]	4.555	5.249	3.589	4.320	3.396	3.627
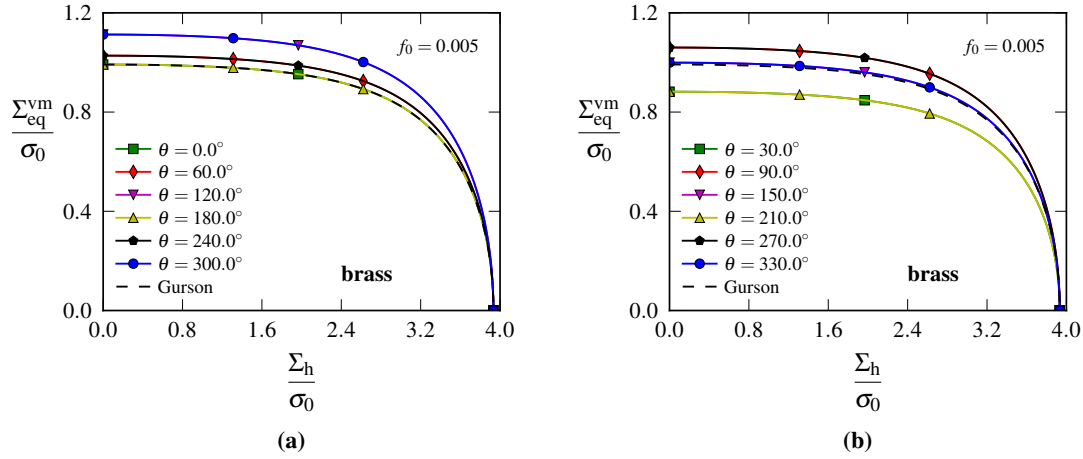
Figure 12: Initial yield loci for the brass texture in the case of (a) generalized axisymmetric and (b) generalized shear stress states with an initial porosity $f_0 = 0.005$. The initial yield locus for the isotropic Gurson-Tvergaard model with the calibrated q_i constants is indicated by a dashed line.

deviatoric angles, which is in accordance with the shape of the matrix yield surfaces shown in Figure 1. In the case of vanishing hydrostatic tension, the porous plasticity yield surfaces scale with the matrix material according to

$$\Sigma_{eq} = (1 - q_1 f)\sigma_M \tag{27}$$

At the other extreme, meaning a fully hydrostatic stress state, the yield function in Equation (21) reduces to

$$|\Sigma_h| = -\frac{2\sigma_M}{3q_2} \ln(q_1 f) \tag{28}$$

and there is no effect of the plastic anisotropy. In this case, all deviatoric angles reduce to the same yielding point, as seen from Figure 12. The hydrostatic limit value is strongly dependent upon the set of q_i parameters adopted, which is readily inferred from Equation (28), and the various textures will generally differ depending upon the calibrated material constants.

4.4. Performance assessment

The material response obtained with the calibrated porous plasticity model is compared to the unit cell calculations in Figures 13 and 14. These curves are for the brass texture in the case of a stress triaxiality of $T = 1$, but for all the imposed deviatoric angles. Numerical results for the other textures are shown in Appendix C, but will not be discussed further in this paper. However, results for the brass texture are representative for the remaining textures, which is inferred from the error estimates listed in Table 3.

Figures 13a and 13b show a comparison of the equivalent stress-strain response between the unit cell (solid lines) and the porous plasticity model (dashed lines) in the case of axisymmetric (GT_i, GC_i) and shear (GS_i) loading states,
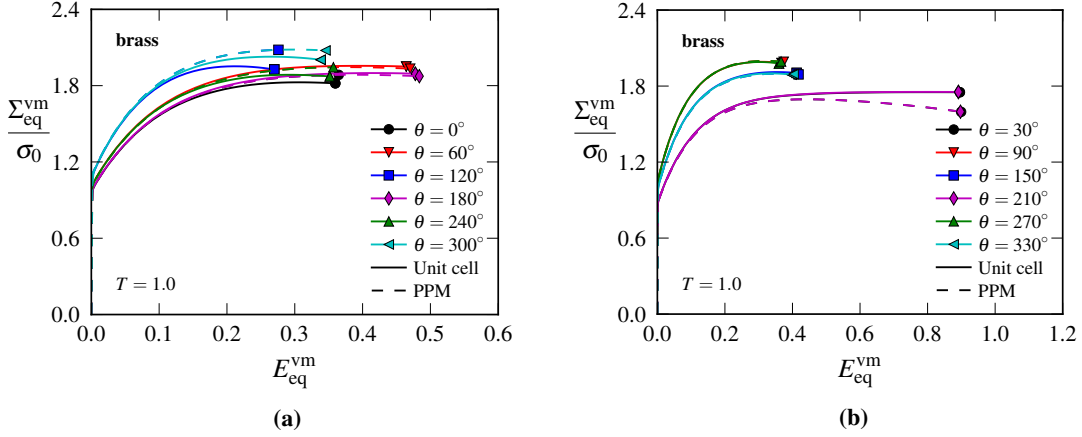
Figure 13: Equivalent stress data from the unit cell simulations (solid lines) are compared with the results of the calibrated porous plasticity model (dashed lines). The shown curves are for the brass texture in the case of $T = 1$ and (a) generalized axisymmetric states, and (b) generalized shear states. Some data points beyond the peak stress have been included.

respectively. These figures demonstrate that, for this texture with the imposed triaxiality of $T = 1$, we have rather good correspondence between the unit cell and the constitutive model for the generalized compression states. Both GC_1 ($\theta = 60°$) and GC_2 ($\theta = 180°$) conform exactly to the FE unit cell simulations. However, there is a discrepancy for GC_3 ($\theta = 300°$) where the peak stress, and thus the onset of material softening, is not adequately captured by the PPM as compared to the corresponding unit cell simulation. Moreover, states of generalized tension are not accurately predicted by the model, for which it is seen that the model underestimates the degree of material softening. This is also reflected by the void growth curves in Figure 14a in which the void growth rate calculated by the PPM is too low. Generalized shear loading states provide overall better predictions, and we see that the model is able to capture the unit cell curves in most cases. That is, however, with the exception of GS_1 ($\theta = 30°$) and GS_4 ($\theta = 210°$), for which the PPM predicts premature material softening.

The same tendencies are observed for the void growth, as seen from Figures 14a and 14b. Again, the generalized tension states suffer from inaccurate predictions, while compressive and shearing states yield enhanced predictions with the previously mentioned exceptions for GC_3, GS_1, and GS_4. It should be noted that the discrepancies observed in the void growth curves are in general more prominent than for the corresponding equivalent stress-strain curves, which is reflected by the corresponding error estimates given in Table 3. This implies that although the macroscopic response might be quite well captured in terms of stress, it could still give inaccurate predictions in terms of porosity. This is a mere effect of the porous plasticity model not being sufficiently refined to realistically account for the evolution of the microstructure. However, including more parameters and microstructural effects into the modelling framework also comes at the expense of additional complexity in formulation, implementation and calibration.

By close inspection of the curves in Figures 13 and 14 we also see that stress states that appear similar on the yield surfaces in Figure 1 exhibit the same response in the porous plasticity model. This is indicated by for instance loading cases GT_2 ($\theta = 120°$) and GC_3 ($\theta = 300°$), or GS_1 ($\theta = 30°$) and GS_4 ($\theta = 210°$). However, the unit cell calculations do not necessarily exhibit identical macroscopic response for stress states that appear similar on the matrix yield surfaces. This was discussed in the previous section and stems from the non-uniform spatial fields, originating in the vicinity of the void. The homogenized material model (PPM) is not able to account for these heterogeneities since it smears out the mechanical field variables within the material element. Ultimately, this generates differences between the PPM and the unit cell calculations. Additionally, Lode effects that give rise to different void shape evolution in the unit cell simulations are not reflected by the PPM since it is based on the assumption of spherical void growth. As a result, stress states that have the same flow stress and yield surface normal will be similar in terms of void growth.

Although we observe more pronounced differences for the model predictions in some loading cases than others, it seems futile to dwell on potential reasons for why these particular loading directions lead to a greater mismatch since this conclusion is dependent upon the texture under consideration. Also, it is important to keep in mind that the porous plasticity model has been calibrated on the basis of all imposed stress states. By way of consequence, some
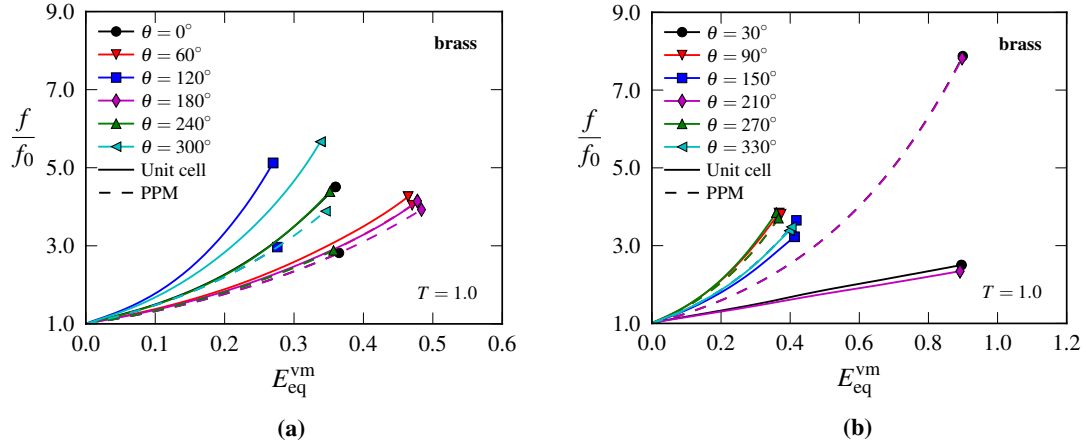
22

Figure 14: Void growth from the unit cell simulations (solid lines) are compared with the results of the calibrated porous plasticity model (dashed lines). The shown curves are for the brass texture in the case of $T = 1$ and (a) generalized axisymmetric states, and (b) generalized shear states. Some data points beyond the peak stress have been included.

loading directions might provide poor approximations to the unit cell response while other directions could give perfect correspondence. This is what we observe in the current study. One comment worthwhile in that respect is that for many practical situations there is no need to calibrate the porous plasticity model under such a wide variety of stress states. If we for instance are interested in the typical conditions prevailing during sheet metal forming, it might be sufficient for the material model to perform well under stress states close to biaxial tension, or at least plane stress states. This significantly narrows down the number of distinct target curves in the optimization procedure, and will most likely provide a set of q_i parameters that gives sufficiently accurate predictions for the application domain.
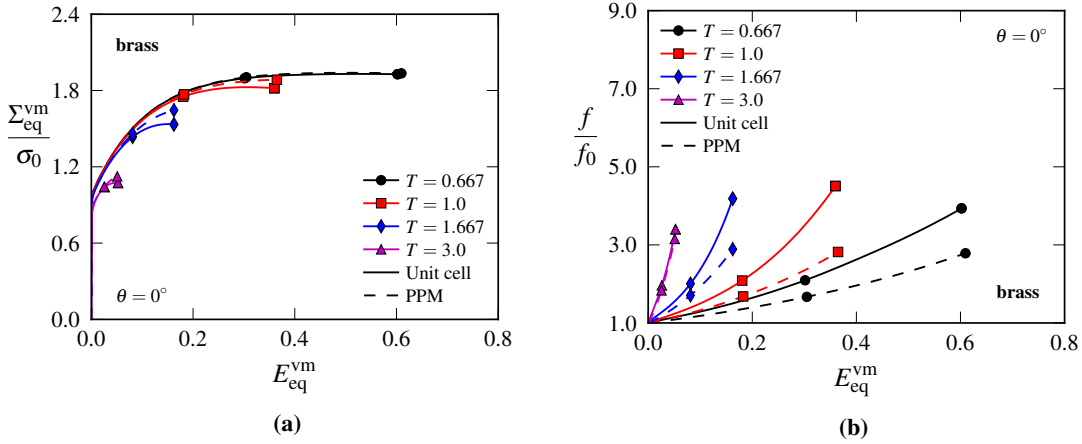

Figure 15: Material response in terms of (a) equivalent stress and (b) void growth is shown for different stress triaxialities with a generalized tension loading of $\theta = 0°$. Solid lines correspond to unit cell data while dashed lines correspond to the porous plasticity model. The data points pertain to the brass texture.

The previous figures showed only results for the same triaxiality ratio. However, it is imperative that the material model also performs well for different triaxiality levels. Figures 15, 16, and 17 compare the porous plasticity model to the unit cell simulations for $T = 2/3, 1, 5/3,$ and 3 in the case of deviatoric states corresponding to GT_1 ($\theta = 0°$), GS_1 ($\theta = 30°$), and GC_1 ($\theta = 60°$), respectively. On the one hand, we find the results in the low stress triaxiality range somewhat inaccurate for all these deviatoric angles, as inferred from the results pertaining to $T = 2/3$ and 1. Again, the largest discrepancy is observed for the void growth curves. The reasons for the lack of accuracy in the low triaxiality
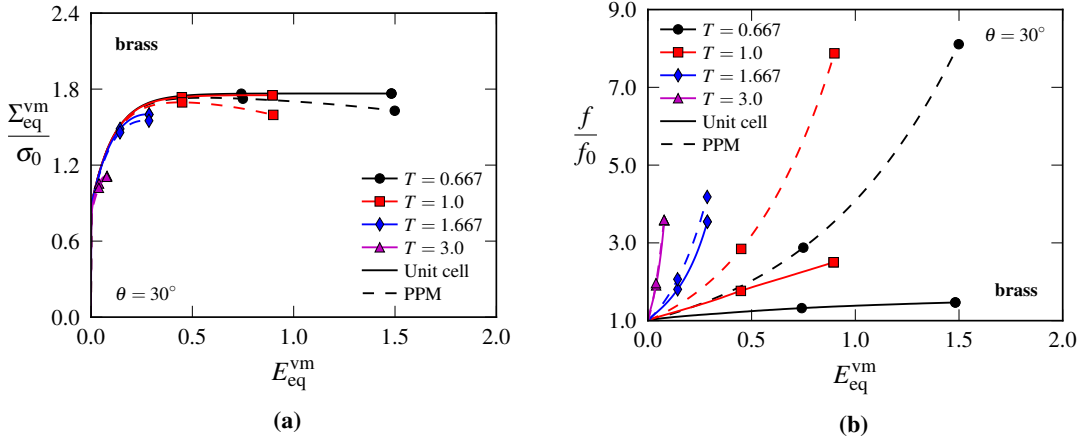
Figure 16: Material response in terms of (a) equivalent stress and (b) void growth is shown for different stress triaxialities with a generalized shear loading of $\theta = 30°$. Solid lines correspond to unit cell data while dashed lines correspond to the porous plasticity model. The data points pertain to the brass texture.

range are associated with the non-spherical void evolution and its interplay with the matrix anisotropy. On the other hand, the accordance with the unit cell calculations is rather good in the high stress triaxiality regime, indicated by the numerical data for $T = 5/3$ and $T = 3$, for all displayed deviatoric angles. This is in agreement to what is previously established in the literature, and to the fact that the original Gurson model yields the exact solution to the representative volume element under purely hydrostatic loading. It should be noted that the use of the q_i parameters in general impairs the predictions under high stress triaxialities, but this effect is not too prominent for the optimized set of material parameters in the current work. Also, it is likely that even higher stress triaxialities must be applied in order for this deficiency to become apparent. Such confined stress states are rarely encountered in practical applications.

4.5. Final comments on the porous plasticity model performance

Based on the results presented herein, we are inclined to believe that this heuristic extension of the Gurson model can be employed to predict the homogenized behaviour of a voided FCC polycrystalline solid exhibiting strongly anisotropic plastic yielding. We have shown that the constitutive model is able to replicate the unit cell predictions quite well in the case of the brass texture. Numerical data for the other textures were not discussed for the sake of brevity, but the performance of the PPM for the brass texture is representative for the remaining textures as shown in Appendix C. Some of these textures are quite extreme, with both severe anisotropy and a high curvature of the yield surface, and the ability to capture the unit cell response for these textures entails that more moderate textures should also be well captured. However, for the lower stress triaxialities, the mismatch between the porous plasticity model and the unit cell calculations is more prominent. An extension of the porous plasticity model in which the void growth rate explicitly accounts for effects of the third deviatoric stress invariant is judged likely to at least partly remedy this deficiency. Potential models that account for such effects have been proposed in the literature (Nahshon and Hutchinson, 2008; Xue, 2008), in which the void growth is augmented by a term accounting for shearing of voids. This extension is straightforward to include also for the current model, and an examination of such a modification is indeed interesting for future work.

We note that all the results presented herein pertain to deformations prior to the onset of void coalescence. This last stage of the ductile failure process is immensely important to describe in order to realistically simulate crack propagation and final fracture. We have not made any efforts in the present study to investigate such methods, but we note that there have been proposed a number of models in the literature that can be used to model void coalescence which can be used to extend the current constitutive framework. The interested reader is referred to for instance Pardoen and Hutchinson (2000) and Tekoğlu et al. (2012) and the references therein.
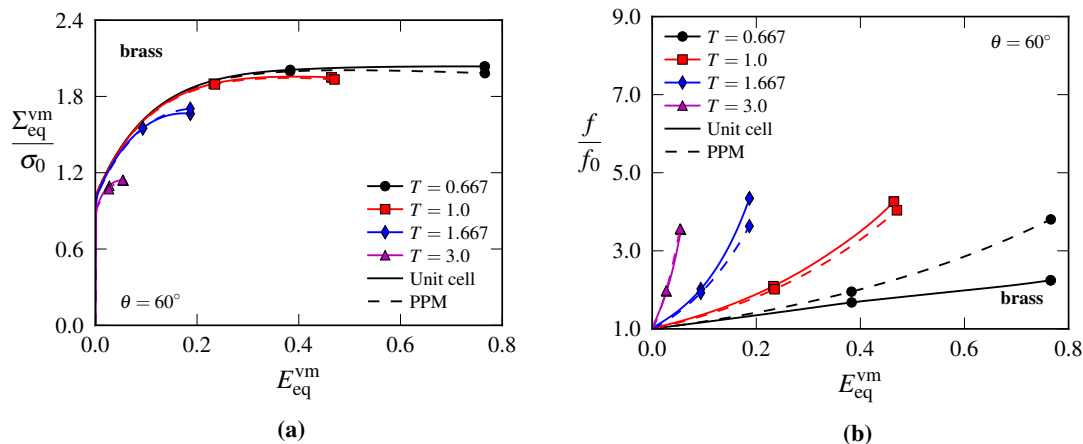
24

Figure 17: Material response in terms of (a) equivalent stress and (b) void growth is shown for different stress triaxialities with a generalized compression loading of $\theta = 60°$. Solid lines correspond to unit cell data while dashed lines correspond to the porous plasticity model. The data points pertain to the brass texture.

5. Concluding remarks

Unit cell simulations of voided anisotropic materials were conducted for a wide range of realistic macroscopic stress states. The anisotropy parameters of the phenomenological yield criterion were taken to represent strong, generic textures for FCC metals. The numerical results revealed the pronounced dependence of the unit cell response upon the orientation of the major principal stress direction relative to the material axes, which implies the influence of the matrix anisotropy. This was demonstrated in terms of both the void growth and the void shape evolution. It was found that, based on the adopted definition of the stress triaxiality, the void growth was largely dependent upon the radius of the yield surface in the deviatoric plane for a given stress state. Moreover, the direction of plastic flow had a marked influence on the void growth, both in terms of shape evolution and growth rate. These effects are linked to the matrix anisotropy. Furthermore, the observation that the void growth rate is dependent upon the deviatoric angle when the loading state is otherwise identical was also apparent from the numerical results.

A heuristic extension of the Gurson model accounting for a plastically anisotropic matrix was proposed and calibrated based on the unit cell data. The model was seen to capture the main trends from the cell calculations. Thus, based on the notion that the unit cell is an adequate representation of the voided polycrystalline solid at the microscale, the porous plasticity model is judged applicable for higher-scale simulations where it is desirable to account for progressive damage and softening due to void growth. However, we also note that in order to further enhance the model predictions it is necessary to include some correction for void shape effects.

A numerical framework to prescribe proportional loading paths to the unit cell in the case of anisotropic material behaviour was proposed. This procedure makes use of nonlinear kinematic constraints to maintain the prescribed macroscopic stress state throughout the loading step. We also outlined a method to prescribe a proportional loading path to the homogenized porous plasticity model, which was necessary to calibrate this model from the unit cell results.

References

Abaqus, 2013. Version 6.13. Dassault Systèmes Simulia Corp., Providence, RI, USA.

Achani, D., Hopperstad, O. S., Lademo, O. G., 2009. Influence of advanced yield criteria on predictions of plastic anisotropy for aluminium alloy sheets. International Journal of Material Forming 2, 487–490.

Achani, D., Lademo, O. G., Engler, O., Hopperstad, O. S., 2011. Evaluation of constitutive models for textured aluminium alloys using plane-strain tension and shear tests. International Journal of Material Forming 4, 227–241.

Barlat, F., Aretz, H., Yoon, J. W., Karabin, M. E., Brem, J. C., Dick, R. E., 2005. Linear transfomation-based anisotropic yield functions. International Journal of Plasticity 21, 1009–1039.

Barlat, F., Lege, D. J., Brem, J. C., 1991. A six-component yield function for anisotropic materials. International Journal of Plasticity 7, 693–712.

Barlat, F., Richmond, O., 1987. Prediction of Tricomponent Plane Stress Yield Surfaces and Associated Flow and Failure Behavior of Strongly Textured F.C.C. Polycrystalline Sheets. Materials Science and Engineering 95, 15–29.

Barsoum, I., Faleskog, J., 2007. Rupture mechanisms in combined tension and shear-Micromechanics. International Journal of Solids and Structures 44, 5481–5498.

Belytschko, T., Liu, W. K., Moran, B., 2000. Nonlinear Finite Elements For Continua And Structures.

Benzerga, A. A., Besson, J., 2001. Plastic potentials for anisotropic porous solids. European Journal of Mechanics - A/Solids 20, 397–434.

Benzerga, A. A., Besson, J., Batisse, R., Pineau, A., 2002. Synergistic effects of plastic anisotropy and void coalescence on fracture mode in plane strain. Modelling and Simulation in Materials Science and Engineering 10, 73–102.

Benzerga, A. A., Besson, J., Pineau, A., 2004. Anisotropic ductile fracture: Part II: Theory. Acta Materialia 52, 4639–4650.

Benzerga, A. A., Leblond, J. B., 2010. Ductile Fracture by Void Growth to Coalescence. Advances in Applied Mechanics 44, 169 —- 305.

Benzerga, A. A., Leblond, J. B., Needleman, A., Tvergaard, V., 2016. Ductile Failure Modeling. International Journal of Fracture 201, 29–80.

Besson, J., 2010. Continuum Models of Ductile Fracture: A Review. International Journal of Damage Mechanics 19 (1), 3–52.

Bishop, J. F. W., Hill, R., 1951. XLVI. A theory of the plastic distortion of a polycrystalline aggregate under combined stresses. The London, Edinburgh, and Dublin Philosophical Magazine and Journal of Science 42, 414—-427.

Bron, F., Besson, J., 2004. A yield function for anisotropic materials Application to aluminum alloys. International Journal of Plasticity 20 (4-5), 937–963.

Brunet, M., Mguil, S., Morestin, F., 1998. Analytical and experimental studies of necking in sheet metal forming processes. Journal of Materials Processing Technology 80–81, 40—-46.

Brünig, M., Chyra, O., Albrecht, D., Driemeier, L., Alves, M., 2008. A ductile damage criterion at various stress triaxialities. International Journal of Plasticity 24, 1731–1755.

Cazacu, O., Plunkett, B., Barlat, F., 2006. Orthotropic yield criterion for hexagonal closed packed metals. International Journal of Plasticity 22, 1171–1194.

Chen, Z., Dong, X., 2009. The GTN damage model based on Hill'48 anisotropic yield criterion and its application in sheet metal forming. Computational Materials Science 44, 1013–1021.

Cheng, L., Guo, T., 2007. Void interaction and coalescence in polymeric materials. International Journal of Solids and Structures 44 (6), 1787–1808.

Chien, W. Y., Pan, J., Tang, S. C., 2001. Modified Anisotropic Gurson Yield Criterion for Porous Ductile Sheet Metals. Journal of Engineering Materials and Technology 123, 409–416.

Chow, C. L., Wang, J., 1987. An anisotropic theory of continuum damage mechanics for ductile fracture. Engineering Fracture Mechanics 27, 547–558.

Dæhli, L. E. B., Børvik, T., Hopperstad, O. S., 2016a. Influence of loading path on ductile fracture of tensile specimens made from aluminium alloys. International Journal of Solids and Structures 88-89, 17–34.

Dæhli, L. E. B., Faleskog, J., Børvik, T., Hopperstad, O. S., 2016b. Unit cell simulations and porous plasticity modelling for recrystallization textures in aluminium alloys. Procedia Structural Integrity 2, 2535—-2542.

Doege, E., Seibert, D., 1995. Prediction of necking and wrinkling in sheet-metal forming. Journal of Materials Processing Technology 50, 197–206.

Engler, O., Randle, V., 2010. Introduction to texture analysis: Macrotexture, Microtexture and Orientation Mapping. CRC Press.

Faleskog, J., Gao, X., Shih, C. F., 1998. Cell model for nonlinear fracture analysis – I. Micromechanics calibration. International Journal of Fracture 89, 355–373.

Fourmeau, M., Børvik, T., Benallal, A., Hopperstad, O. S., 2013. Anisotropic failure modes of high-strength aluminium alloy under various stress states. International Journal of Plasticity 48, 34–53.

Gao, X., Zhang, T., Zhou, J., Graham, S. M., Hayden, M., Roe, C., 2011. On stress-state dependent plasticity modeling: Significance of the hydrostatic stress, the third invariant of stress deviator and the non-associated flow rule. International Journal of Plasticity 27, 217–231.

Gologanu, M., Leblond, J. B., Devaux, J., 1993. Approximate models for ductile metals containing non-spherical voids – Case of axisymmetric prolate ellipsoidal cavities. Journal of the Mechanics and Physics of Solids 41, 1723–1754.

Grange, M., Besson, J., Andrieu, E., 2000. An anisotropic Gurson type model to represent the ductile rupture of hydrided Zircaloy-4 sheets. International Journal of Fracture 105, 273–293.

Gurson, A. L., 1977. Continuum Theory of Ductile Rupture by Void Nucelation and Growth: Part I – Yield Criteria and Flow Rules for Porous Ductile Media. Journal of Engineering Materials and Technology 99, 2—-15.

Han, X., Besson, J., Forest, S., Tanguy, B., Bugat, S., 2013. A yield function for single crystals containing voids. International Journal of Solids and Structures 50, 2115–2131.

Hashin, Z., Shtrikman, S., 1963. A variational approach to the theory of the elastic behaviour of multiphase materials. Journal of the Mechanics and Physics of Solids 11, 127–140.

Hershey, A. V., 1954. The plasticity of an isotropic aggregate of anisotropic face-centered cubic crystals. Journal of Applied Mechanics 21, 241–249.

Hill, R., 1948. A theory of the yielding and plastic flow of anisotropic metals. Proceedings of the Royal Society of London. Series A, Mathematical and Physical Sciences 193, 281–297.

Hill, R., 1967. The essential structure of constitutive laws for metal composites and polycrystals. Journal of the Mechanics and Physics of Solids 15, 79–95.

Hosford, W. F., 1972. A Generalized Isotropic Yield Criterion. Journal of Applied Mechanics 39, 607–609.

Hutchinson, J., 1964. Plastic deformation of B.C.C. polycrystals. Journal of the Mechanics and Physics of Solids 12, 25–33.

Iadicola, M. A., Foecke, T., Banovic, S. W., 2008. Experimental observations of evolving yield loci in biaxially strained AA5754-O. International Journal of Plasticity 24, 2084–2101.

Jordon, J. B., Horstemeyer, M. F., Solanki, K., Bernard, J. D., Berry, J. T., Williams, T. N., 2009. Damage characterization and modeling of a 7075-T651 aluminum plate. Materials Science and Engineering A 527, 169–178.

Karafillis, A., Boyce, M. C., 1993. A general anisotropic yield criterion using bounds and a transformation weighting tensor. Journal of the Mechanics and Physics of Solids 41, 1859–1886.

Keralavarma, S. M., Benzerga, A. A., 2010. A constitutive model for plastically anisotropic solids with non-spherical voids. Journal of the Mechanics and Physics of Solids 58, 874–901.

Keralavarma, S. M., Hoelscher, S., Benzerga, A. A., 2011. Void growth and coalescence in anisotropic plastic solids. International Journal of Solids and Structures 48, 1696–1710.

Kim, J., Gao, X., Srivatsan, T. S., 2004. Modeling of void growth in ductile solids: Effects of stress triaxiality and initial porosity. Engineering Fracture Mechanics 71, 379–400.

Leblond, J. B., Perrin, G., Suquet, P., 1994. Exact results and approximate models for porous viscoplastic solids. International Journal of Plasticity 10, 213–235.

Liao, K. C., Pan, J., Tang, S. C., 1997. Approximate yield criteria for anisotropic porous ductile sheet metals. Mechanics of Materials 26, 213 —-226.

Liu, Z. G., Wong, W. H., Guo, T. F., 2016. Void behaviors from low to high triaxialities: Transition from void collapse to void coalescence. International Journal of Plasticity 84, 183–202.

Luo, M., Dunand, M., Mohr, D., 2012. Experiments and modeling of anisotropic aluminum extrusions under multi-axial loading - Part II: Ductile fracture. International Journal of Plasticity 32-33, 36–58.

Mandel, J., 1966. Contribution théorique à l'étude de l'écrouissage et des lois de l'écoulement plastique. Springer Berlin Heidelberg, Berlin, Heidelberg, pp. 502–509.

Monchiet, V., Cazacu, O., Charkaluk, E., Kondo, D., 2008. Macroscopic yield criteria for plastic anisotropic materials containing spheroidal voids. International Journal of Plasticity 24, 1158–1189.

Morin, L., Leblond, J. B., Kondo, D., 2015. A Gurson-type criterion for plastically anisotropic solids containing arbitrary ellipsoidal voids. International Journal of Solids and Structures 77, 86–101.

Morin, L., Leblond, J. B., Tvergaard, V., 2016. Application of a model of plastic porous materials including void shape effects to the prediction of ductile failure under shear-dominated loadings. Journal of the Mechanics and Physics of Solids 94, 148–166.

Nahshon, K., Hutchinson, J. W., 2008. Modification of the Gurson Model for shear failure. European Journal of Mechanics - A/Solids 27, 1–17.

Pardoen, T., 2006. Numerical simulation of low stress triaxiality ductile fracture. Computers & Structures 84, 1641–1650.

Pardoen, T., Hutchinson, J. W., 2000. Extended model for void growth and coalescence. Journal of the Mechanics and Physics of Solids 48, 2467–2512.

Plunkett, B., Cazacu, O., Barlat, F., 2008. Orthotropic yield criteria for description of the anisotropy in tension and compression of sheet metals. International Journal of Plasticity 24, 847–866.

Prat, F., Grange, M., Besson, J., Andrieu, E., 1998. Behavior and Rupture of Hydrided ZIRCALOY-4 Tubes and Sheets. Metallurgical and Materials Transactions A 29A, 1643—-1651.

Saai, A., Dumoulin, S., Hopperstad, O. S., Lademo, O. G., 2013. Simulation of yield surfaces for aluminium sheets with rolling and recrystallization textures. Computational Materials Science 67, 424–433.

Saai, A., Hopperstad, O. S., Dumoulin, S., Tabourot, L., 2014. Numerical Study on the Influence of Crystallographic Texture and Grain Shape on the Yield Surface of Textured Aluminum Sheet Material. Materials Science Forum 794-796, 584–589.

Scipy, 2016. Optimization and root finding.
URL http://docs.scipy.org/doc/scipy/reference/optimize.html

Shinohara, Y., Madi, Y., Besson, J., 2016. Anisotropic ductile failure of a high-strength line pipe steel. International Journal of Fracture 197, 127 —-145.

Srivastava, A., Needleman, A., 2013. Void growth versus void collapse in a creeping single crystal. Journal of the Mechanics and Physics of Solids 61, 1169–1184.

Srivastava, A., Needleman, A., 2015. Effect of crystal orientation on porosity evolution in a creeping single crystal. Mechanics of Materials 90, 10–29.

Steglich, D., Wafai, H., Besson, J., 2010. Interaction between anisotropic plastic deformation and damage evolution in Al 2198 sheet metal. Engineering Fracture Mechanics 77 (17), 3501–3518.

Stewart, J. B., Cazacu, O., 2011. Analytical yield criterion for an anisotropic material containing spherical voids and exhibiting tension-compression asymmetry. International Journal of Solids and Structures 48, 357–373.

Stout, M. G., Hecker, S. S., Bourcier, R., 1983. An Evaluation of Anisotropic Effective Stress-Strain Criteria for the Biaxial Yield and Flow of 2024 Aluminum Tubes. Journal of Engineering Materials and Technology 105, 242–249.

Tekoğlu, C., Leblond, J.-B., Pardoen, T., 2012. A criterion for the onset of void coalescence under combined tension and shear. Journal of the Mechanics and Physics of Solids 60, 1363–1381.

Tvergaard, V., 1981. Influence of voids on shear band instabilities under plane strain conditions. International Journal of Fracture 17, 389–407.

Vadillo, G., Fernández-Sáez, J., 2009. An analysis of Gurson model with parameters dependent on triaxiality based on unitary cells. European Journal of Mechanics - A/Solids 28, 417–427.

Wang, D. A., Pan, J., Liu, S.-D., 2004. An Anisotropic Gurson Yield Criterion for Porous Ductile Sheet Metals with Planar Anisotropy. International Journal of Damage Mechanics 13, 7–33.

Westermann, I., Pedersen, K. O., Furu, T., Børvik, T., Hopperstad, O. S., 2014. Effects of particles and solutes on strength, work-hardening and ductile fracture of aluminium alloys. Mechanics of Materials 79, 58–72.

Wong, W. H., Guo, T. F., 2015. On the energetics of tensile and shear void coalescences. Journal of the Mechanics and Physics of Solids 82, 259–286.

Woodthorpe, J., Pearce, R., 1970. The anomalous behaviour of aluminium sheet under balanced biaxial tension. International Journal of Mechanical

Sciences 12, 341–347.

Xue, L., 2008. Constitutive modeling of void shearing effect in ductile fracture of porous materials. Engineering Fracture Mechanics 75, 3343–3366.

Yerra, S. K., Tekoglu, C., Scheyvaerts, F., Delannay, L., Van Houtte, P., Pardoen, T., 2010. Void growth and coalescence in single crystals. International Journal of Solids and Structures 47, 1016–1029.

Yoshida, K., Kuroda, M., 2012. Comparison of bifurcation and imperfection analyses of localized necking in rate-independent polycrystalline sheets. International Journal of Solids and Structures 49, 2073–2084.

Zhang, K., Bai, J. B., François, D., 2001. Numerical analysis of the influence of the Lode parameter on void growth. International Journal of Solids and Structures 38, 5847–5856.

Appendix A. Yld2004-18p model parameters

Table A.1: List of the plastic anisotropy coefficients entering the Yld2004-18p criterion for the different textures.

Texture	Brass	Copper	Cube	Goss	S	Random
m	13.02	20.14	18.22	17.039	14.19	9.57
$\hat{A}_{1122}^{(1)}$	0.981	0.896	1.008	0.909	0.832	0.904
$\hat{A}_{1133}^{(1)}$	1.088	0.996	0.656	1.003	0.644	0.918
$\hat{A}_{2211}^{(1)}$	0.616	1.125	1.107	-0.169	0.515	1.174
$\hat{A}_{2233}^{(1)}$	0.363	1.227	0.711	0.340	0.904	1.119
$\hat{A}_{3311}^{(1)}$	0.726	0.913	-0.132	0.568	0.811	0.999
$\hat{A}_{3322}^{(1)}$	0.712	0.742	-0.080	0.250	0.979	0.957
$\hat{A}_{1212}^{(1)}$	0.832	0.878	1.098	0.780	1.107	1.023
$\hat{A}_{2323}^{(1)}$	1.000	1.000	1.000	1.000	1.000	1.000
$\hat{A}_{3131}^{(1)}$	1.000	1.000	1.000	1.000	1.000	1.000
$\hat{A}_{1122}^{(2)}$	0.738	0.932	0.825	1.262	1.372	0.966
$\hat{A}_{1133}^{(2)}$	0.683	1.032	0.764	0.264	1.256	1.021
$\hat{A}_{2211}^{(2)}$	0.930	0.837	0.738	1.174	1.055	0.782
$\hat{A}_{2233}^{(2)}$	1.089	0.560	1.135	1.167	0.833	0.877
$\hat{A}_{3311}^{(2)}$	1.077	1.067	1.406	1.085	0.869	1.026
$\hat{A}_{3322}^{(2)}$	0.922	1.088	1.339	0.931	1.107	0.955
$\hat{A}_{1212}^{(2)}$	1.212	1.567	0.329	0.634	1.083	0.946
$\hat{A}_{2323}^{(2)}$	1.000	1.000	1.000	1.000	1.000	1.000
$\hat{A}_{3131}^{(2)}$	1.000	1.000	1.000	1.000	1.000	1.000

Appendix B. Control of macroscopic stress state

Appendix B.1. Unit cell

Under the application of uniform boundary conditions at the unit cell edges, the Hill-Mandel homogenization theory (Mandel, 1966; Hill, 1967) entails that the macrosopic deformation power is equal to its volume-averaged counterpart

$$\dot{W}_{\mathrm{d}} = V\boldsymbol{\Sigma} : \mathbf{D} = \int_V \boldsymbol{\sigma} : \mathbf{d}\,\mathrm{d}V \tag{B.1}$$

Using the notation $\{\circ\}$ and $[\circ]$ to indicate vector and matrix quantities, respectively, this may be written on Voigt form such that

$$\dot{W}_{\mathrm{d}} = V\{\boldsymbol{\Sigma}\}^T\{\mathbf{D}\} = V\{\boldsymbol{\Sigma}\}^T[\mathbf{T}]\{\dot{\mathbf{U}}\} \tag{B.2}$$

29

where the matrix relation $\{\mathbf{D}\} = [\mathbf{T}]\{\dot{\mathbf{U}}\}$ has been invoked to relate the rate-of-deformation vector to the vector containing the displacement rates at the unit cell boundary $\{\dot{\mathbf{U}}\}$. Specifically, the matrix $[\mathbf{T}]$ reads

$$[\mathbf{T}] = \begin{bmatrix} \dfrac{1}{l_1} & 0 & 0 \\ 0 & \dfrac{1}{l_2} & 0 \\ 0 & 0 & \dfrac{1}{l_3} \end{bmatrix} \tag{B.3}$$

where l_i denotes the current length of the unit cell edges.

Let us now transform the macroscopic stress $\boldsymbol{\Sigma}$ and the rate-of-deformation $\mathbf{D}$ according to

$$\{\boldsymbol{\Sigma}\} = [\mathbf{Q}]\{\tilde{\boldsymbol{\Sigma}}\} \quad \wedge \quad \{\mathbf{D}\} = [\mathbf{Q}]\{\tilde{\mathbf{D}}\} \tag{B.4}$$

where $\tilde{\boldsymbol{\Sigma}}$ and $\tilde{\mathbf{D}}$ pertain to the transformed system. This transformation is taken on a form such that a uniaxial stress state prevails in the transformed system, and which renders the deformation power equal in both systems. Hence, we must have from Equation (B.2) that $V\{\boldsymbol{\Sigma}\}^T\{\mathbf{D}\} = V\{\tilde{\boldsymbol{\Sigma}}\}^T\{\tilde{\mathbf{D}}\}$. An implication of the above is that the transformation matrix should be orthogonal, such that $[\mathbf{Q}]^T[\mathbf{Q}] = [\mathbf{1}]$, thus immediately fulfilling the equivalence in deformation power between the two coordinate systems. Further, we use the transformation in Equation (B.4) to write that

$$\dot{W}_{\mathrm{d}} = V\{\tilde{\boldsymbol{\Sigma}}\}^T[\mathbf{Q}]^T[\mathbf{T}]\{\dot{\mathbf{U}}\} = \{\tilde{\mathbf{P}}\}^T\{\dot{\tilde{\mathbf{U}}}\} \tag{B.5}$$

where a transformed generalized force vector on the form $\{\tilde{\mathbf{P}}\} = V\{\tilde{\boldsymbol{\Sigma}}\} = V[\mathbf{Q}]^T\{\boldsymbol{\Sigma}\}$ has been introduced. Consequently, we find that

$$\{\dot{\tilde{\mathbf{U}}}\} = [\mathbf{Q}]^T[\mathbf{T}]\{\dot{\mathbf{U}}\} \tag{B.6}$$

which constitute a set of non-linear kinematic constraints. Note that the transformed generalized force vector only contains one component which is arbitrarily chosen such that $\tilde{P}_1 \neq 0$ while all the remaining components $\tilde{P}_{i\neq 1} = 0$.

The only remaining part is to obtain the transformation matrix $[\mathbf{Q}]$. For the sake of brevity, we omit the details of the derivation and simply postulate an orthogonal transformation matrix on the form

$$[\mathbf{Q}] = \begin{bmatrix} \beta_1 & \beta_2 & \beta_3 \\ \beta_2 & -\dfrac{\beta_3^2 + \beta_1\beta_2^2}{\beta_2^2 + \beta_3^2} & \dfrac{\beta_2\beta_3\,(1-\beta_1)}{\beta_2^2 + \beta_3^2} \\ \beta_3 & \dfrac{\beta_2\beta_3\,(1-\beta_1)}{\beta_2^2 + \beta_3^2} & -\dfrac{\beta_2^2 + \beta_1\beta_3^2}{\beta_2^2 + \beta_3^2} \end{bmatrix} \tag{B.7}$$

Here, the β_i parameters are explicitly given by

$$\beta_1 = \frac{\psi_1}{\bar{\psi}}, \quad \beta_2 = \frac{\psi_2}{\bar{\psi}}, \quad \beta_3 = \frac{\psi_3}{\bar{\psi}}, \quad \bar{\psi} = \sqrt{\psi_1^2 + \psi_2^2 + \psi_3^2} \tag{B.8}$$

where the stress ratios ψ_i are given by Equation (14). From Equation (B.6) we now find that

$$\{\dot{\mathbf{U}}\} = [\mathbf{T}]^{-1}[\mathbf{Q}]\{\dot{\tilde{\mathbf{U}}}\} \tag{B.9}$$

which may be written on incremental form according to

$$\{\Delta\mathbf{U}\} = [\mathbf{T}]^{-1}[\mathbf{Q}]\{\Delta\tilde{\mathbf{U}}\} \tag{B.10}$$

Inversion of the diagonal matrix $[\mathbf{T}]$ is straightforward, and the three boundary displacement components may be

written out explicitly on the form

$$\Delta U_1 = l_1 \left(\beta_1 \Delta \tilde{U}_1 + \beta_2 \Delta \tilde{U}_2 + \beta_3 \Delta \tilde{U}_3 \right) \tag{B.11a}$$

$$\Delta U_2 = l_2 \left(\beta_2 \Delta \tilde{U}_1 - \frac{\beta_3^2 + \beta_1 \beta_2^2}{\beta_2^2 + \beta_3^2} \Delta \tilde{U}_2 + \frac{\beta_2 \beta_3 (1 - \beta_1)}{\beta_2^2 + \beta_3^2} \Delta \tilde{U}_3 \right) \tag{B.11b}$$

$$\Delta U_3 = l_3 \left(\beta_3 \Delta \tilde{U}_1 + \frac{\beta_2 \beta_3 (1 - \beta_1)}{\beta_2^2 + \beta_3^2} \Delta \tilde{U}_2 - \frac{\beta_2^2 + \beta_1 \beta_3^2}{\beta_2^2 + \beta_3^2} \Delta \tilde{U}_3 \right) \tag{B.11c}$$

The incremental kinematic constraints governed by Equations (B.11a)-(B.11c) are applied to the unit cell boundaries in order to impose a proportional loading path. To this end, we make use of the multi-point constraint (MPC) user subroutine in Abaqus/Standard. In the finite element procedure, these boundary conditions are enforced by prescribing the displacement $\tilde{U}_1$ in a fictitious node located outside the model. The two remaining displacement components $\tilde{U}_2$ and $\tilde{U}_3$ are calculated during the increment by the MPC routine through the constraints on the generalized force components $\tilde{P}_2 = \tilde{P}_3 = 0$. The only parameters needed as user input in the MPC routine are the stress triaxiality T and the deviatoric angle θ, which are further used to calculate the constants β_i entering the transformation matrix. These are then maintained to their prescribed constant values throughout the analyses. The constraint equations are numerically integrated using a mid-point rule, such that

$$\Delta U_i^{(n+1)} = \frac{l_i^{(n+1)} + l_i^{(n)}}{2} \sum_{k=1}^{3} Q_{ik} \Delta \tilde{U}_k^{(n+1)} \tag{B.12}$$

where $(n + 1)$ denotes the current analysis increment. For further details regarding the MPC user subroutine, we refer to the Abaqus user manual (Abaqus, 2013).

Appendix B.2. Homogenized material model

Analogous to the method employed in the unit cell modelling part, see Appendix B.1, the porous plasticity model is driven by homogeneous boundary conditions such that a given proportional loading path prevails. Again, we make use of the stress state representation

$$\Sigma_i = \Sigma_{\text{eq}}^{\text{vm}} \left(\frac{2}{3} \cos \theta_i + T \right) \tag{B.13}$$

with

$$\theta_1 = \theta, \quad \theta_2 = \theta - \frac{2\pi}{3}, \quad \theta_3 = \theta + \frac{2\pi}{3} \tag{B.14}$$

to calculate stress ratios on the form

$$\psi_1 = \frac{\Sigma_1}{\Sigma_{\text{max}}}, \quad \psi_2 = \frac{\Sigma_2}{\Sigma_{\text{max}}}, \quad \psi_3 = \frac{\Sigma_3}{\Sigma_{\text{max}}} \tag{B.15}$$

where $\Sigma_{\text{max}} = \max(\Sigma_1, \Sigma_2, \Sigma_3)$. Using the incremental constitutive relation, assuming that the principal stress and strain increments are adequately described by $\Delta \Sigma = \Delta t \dot{\Sigma}$ and $\Delta E = \Delta t D$, we may write

$$\{\Delta \Sigma\} = \Delta \Sigma_{\text{max}} \{\psi\} = [C^{\text{t}}]\{\Delta E\} \tag{B.16}$$

In this relation, C^{t} is the material tangent stiffness and $\Delta \Sigma_{\text{max}} = \max(\Delta \Sigma_1, \Delta \Sigma_2, \Delta \Sigma_3)$ is the maximum principal stress increment. We note that this maximum stress increment has no importance for the numerical procedure, as will be apparent from what follows. Now, we seek the strain increments ΔE that must be assigned to the homogenized material element to keep the principal stress ratios to their pre-defined values. Taking the inverse of Equation (B.16), these strain increments are estimated during the analysis using the previous tangent stiffness matrix, such that

$$\{\Delta E\}_{n+1} = [C^{\text{t}}]_n^{-1} \{\Sigma\}_{n+1} = (\Delta \Sigma_{\text{max}})_{n+1} [C^{\text{t}}]_n^{-1} \{\psi\} \tag{B.17}$$

where n and $n + 1$ denote the previous and the current increment of the analysis, respectively. The above relation gives the appropriate ratios between the three principal strain components. These are further scaled in order to maintain a fixed equivalent strain increment. The strain increments are then determined from

$$\{\Delta \mathbf{E}\}_{n+1} = \frac{[\mathbf{C}^{\mathrm{t}}]_n^{-1}\{\boldsymbol{\psi}\}}{\|[\mathbf{C}^{\mathrm{t}}]_n^{-1}\{\boldsymbol{\psi}\}\|}\Delta \bar{E} \tag{B.18}$$

where $\Delta \bar{E}$ denotes the desired norm of the prescribed strain increment. Equation (B.18) now constitutes the necessary relations in order to drive the material deformation such that T and θ are maintained constant.

Since the strain increments are explicitly calculated by inversion of the tangent stiffness from the previous time step using a forward-Euler method, it is important that they are kept small. Otherwise, the stress triaxiality and deviatoric angle will drift away from their pre-defined values, leaving the porous plasticity results incompatible with results obtained in the unit cell simulations. We used a total number of 100.000 increments up to the strain at the peak stress of the corresponding unit cell simulations in the porous plasticity calculations. The norm of the prescribed strain increment varies slightly between the different textures and loading states, but is generally on the order of 10^{-6}. It was checked that this number of increments was sufficient through a convergence study. Also, the increments in the elastic domain are stepped down to avoid severe jumps in stress triaxiality and deviatoric angle as the deformation switches from purely elastic to elastic-plastic. Apart from its explicit formulation, the computational framework is now entirely similar to that presented in Appendix B.1. Consequently, we define the stress triaxiality and the deviatoric angle from which the principal stress ratios $\psi_i(T, \theta)$ are computed and the principal strain increments updated. Note that, as in the unit cell study, the material axes are taken to be collinear to the principal axes of stress and strain.

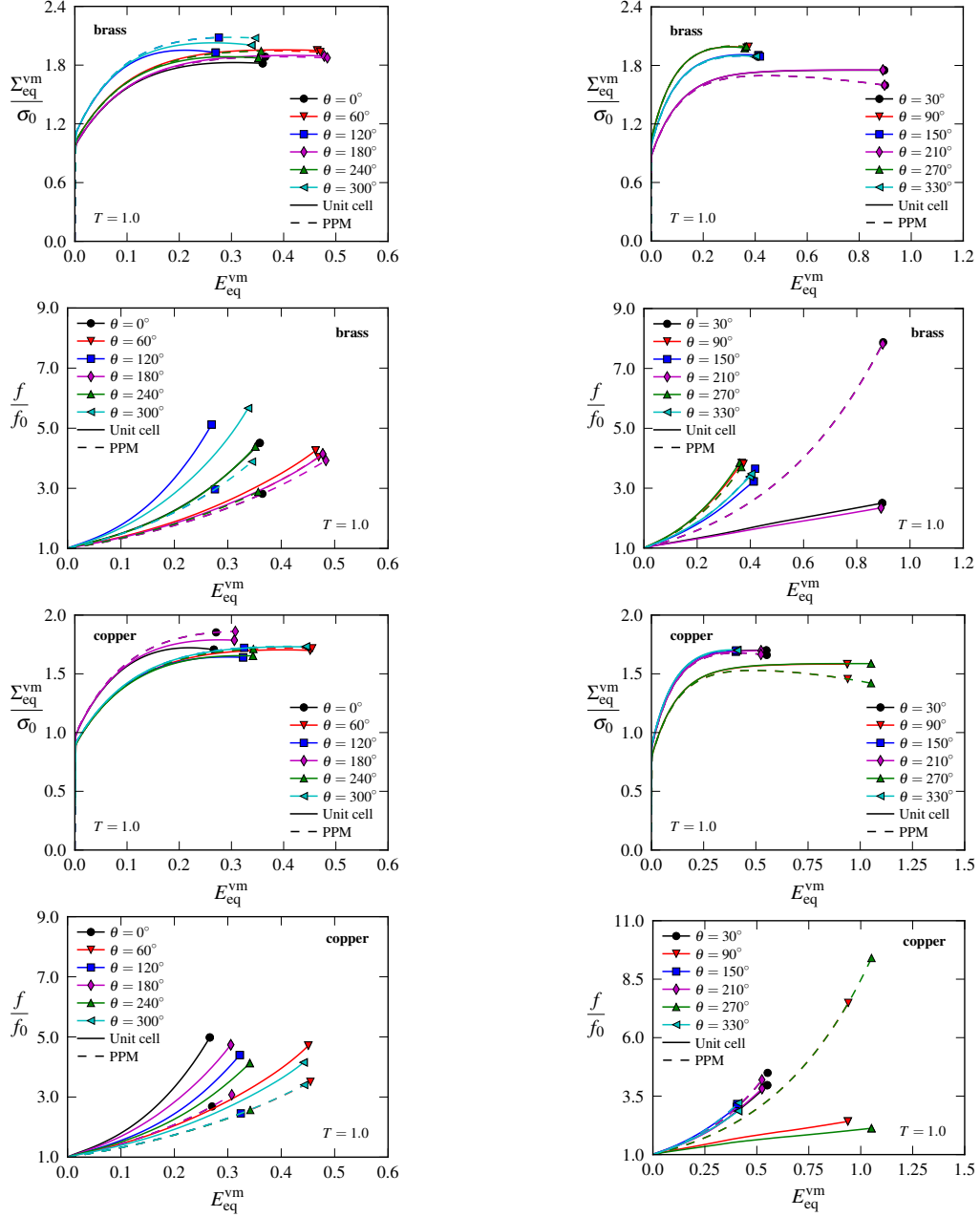# Appendix C. Representative numerical results for all generic textures

Figure C.1: Comparison between unit cell and porous plasticity model response for a stress triaxiality of $T = 1$. Data points slightly beyond the peak stress have been included in the plot.
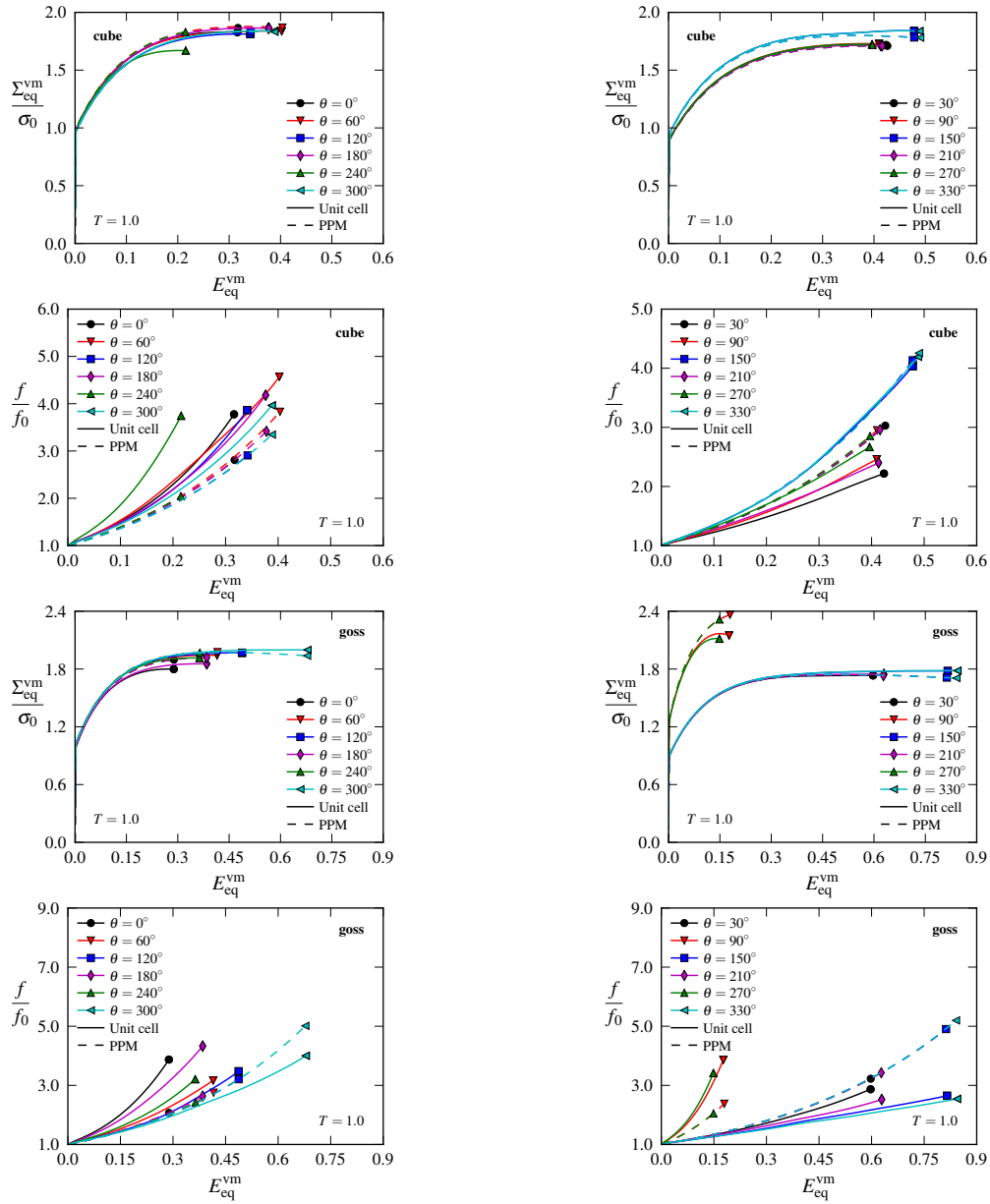
Figure C.2: Comparison between unit cell and porous plasticity model response for a stress triaxiality of $T = 1$. Data points slightly beyond the peak stress have been included in the plot.
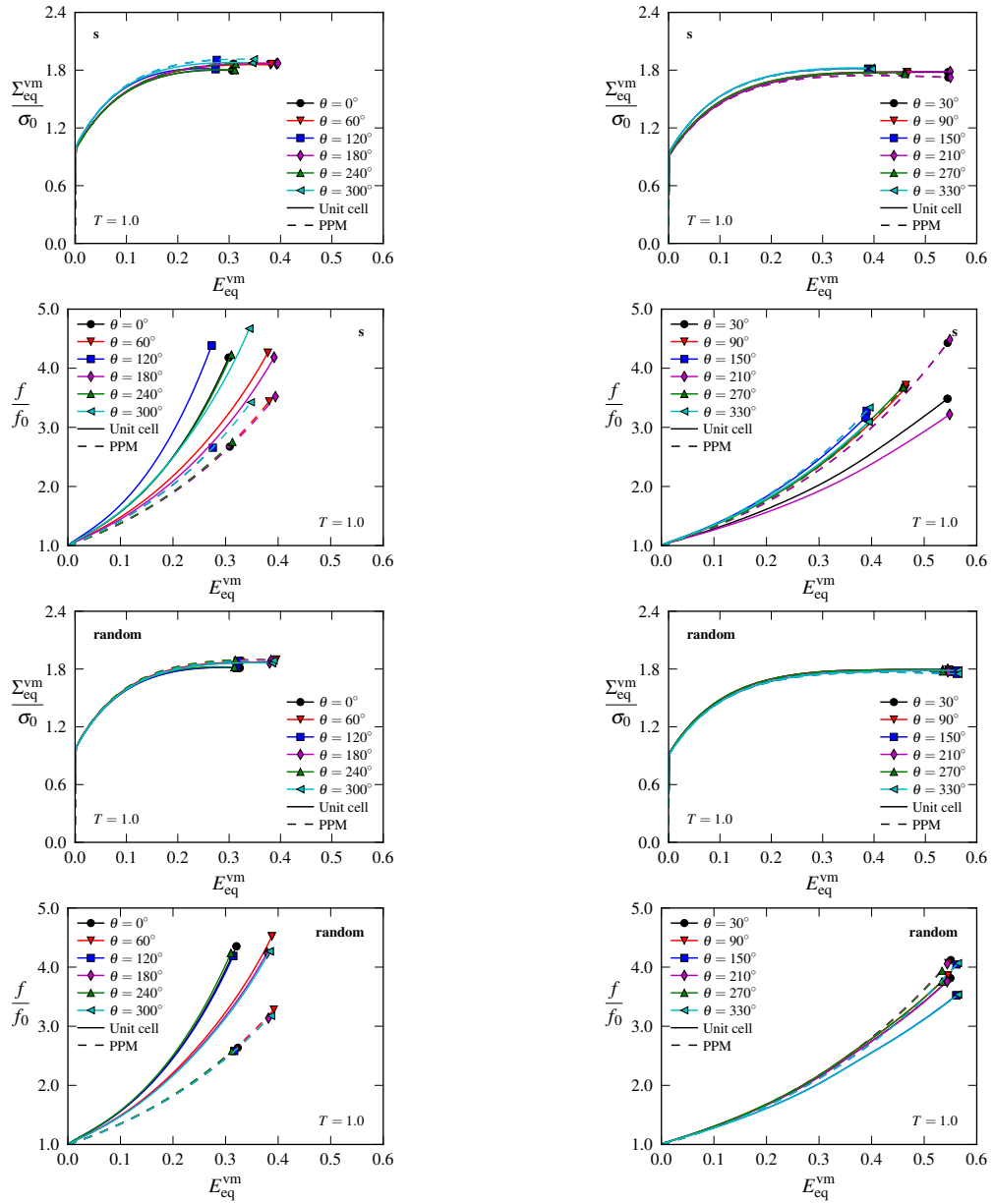
Figure C.3: Comparison between unit cell and porous plasticity model response for a stress triaxiality of $T = 1$. Data points slightly beyond the peak stress have been included in the plot.